

# An Amplification Shaping Framework for Exoskeletal Human Strength Augmentation

Gray Cortright Thomas, *Member, IEEE*, Orion Campbell IV, *Student Member, IEEE*, Nick Nichols, Nicholas Brissoneau, *Student Member, IEEE*, Binghan He, *Student Member, IEEE*, Joshua James, Nicholas Paine, *Member, IEEE*, and Luis Sentis, *Member, IEEE*

**Abstract**—Augmenting the physical strength of a human operator during unpredictable human-directed (volitional) movements is a relevant capability for several proposed exoskeleton applications, including mobility augmentation, manual material handling, tool operation, and mounting useful payloads. Unlike controllers and augmentation systems designed for repetitive tasks (e.g. walking), we approach physical strength augmentation by a task-agnostic method of force amplification—using force/torque sensors at the human-machine interface to estimate the human task force, and then amplifying it with the robot. Coupled stability of the machine with the human motivates our introduction of an amplification shaping framework for the design of safe controllers. To avoid system identification of the operator wearing the exoskeleton, we refine the amplification strategy down to a one-parameter tunable compensator. This amplification controller is integrated into a complete framework for controlling exoskeletons that includes human-led foot transitions, inequality constraints, and a computationally efficient prioritization. A powered lower-body exoskeleton is used to demonstrate behavior of the control framework in a lab environment.

## I. INTRODUCTION

**A**MPLIFICATION of human strength is—among the many possible applications of exoskeletons—an especially interesting feedback control problem. This problem does not appear in exoskeletons that aim to either recover locomotion capability lost to disease [1], [2] or offload the strenuous work of rehabilitation therapy from therapists [3], [4]. Nor is it significant in exoskeletons that aid healthy locomotion with timed power boosts [5], [6], [7]. To amplify human strength is to treat forces of human origin differently from forces of any other origin. And we frame this problem as designing a pair of compliances (or integral-admittances<sup>1</sup>) for the human-side interface of the robot and the environment-side interface of the robot. Amplification control systems are designed to magnify the physical strength of the operator as the operator interacts

G. Thomas, B. He, N. Brissoneau were with the Department of Mechanical Engineering, University of Texas at Austin, Austin, TX, 78712 USA (G. Thomas's e-mail: gcthomas@umich.edu).

L. Sentis was with the Department of Aerospace Engineering, University of Texas at Austin, Austin, TX, 78712 USA (e-mail: lsentis@austin.utexas.edu).

O. Campbell, N. Nichols, J. James, and N. Paine were with Appronik Systems, Inc., Austin, TX, 78758 USA.

Manuscript not yet submitted September 6, 2019; nor revised.

Color versions of one or more of the figures in this paper are available online at <https://ieeexplore.ieee.org>.

Digital Object Identifier XX.XXXX/SRO.2019.XXXXXXX

<sup>1</sup>We prefer ‘compliance’ to ‘integral-admittance’ for brevity, but note that this makes ‘compliance’ a transfer function per force.

with an environment *through the robot* while also reducing the weight and inertia the operator feels from the robot itself. This kind of control allows non-repetitive, unpredictable tasks with unknown payloads.

Lifting *fixed* payloads is a simpler problem. These loads can be lifted by directly compensating their nominal weight with actuator torque commands (the “gravity compensation” strategy). This compensation could be lifting mostly the exoskeleton itself [8], or even offloading the operator’s own bodyweight [9], [10], [11]. In an exoskeleton system that can be easily backdriven by the operator, gravity compensation alone is a passable approach for lifting well-modeled payloads [12]. However, the operator must still accelerate the full inertia, compensate for any model error, and lift any extra payloads themselves. The inertia burden can be lessened by adding positive acceleration feedback [13], [14], but all three issues can be addressed by adding force-feedback-based amplification.

Admittance control for exoskeletons [15], [16], [17], [18] uses force sensor feedback at the human interface<sup>2</sup> in order to increase the human-side compliance, reduce sensitivity to the mass model, and lift unknown loads. But the compliance ‘increase’ is relative to the admittance control plant: a position-controlled robot. Since position-controlled robots have very little compliance [15], [21], the final human-side compliance of an admittance controller is not necessarily an improvement over the torque-controlled gravity compensation strategy. Additionally, the position-controlled plant of the admittance controller will attenuate all external forces acting on the robot. This attenuation typically deprives the operator of force feedback when they interact with the environment.

In order to allow bidirectional transmission of forces to coexist with amplification of human strength, the exoskeleton must transmit both amplified forces from the user to the environment and attenuated forces from the environment to the user. This suggests a force sensor configuration that can distinguish the environment from the user. Directly measuring the robot–environment interface and the robot–human interface with force sensors allowed [22], [23], [24] to control *disparate* admittance behaviors for each interface.<sup>3</sup> But the

<sup>2</sup>Measuring human muscular effort, as can also be accomplished via electromyography (muscle measurement) [19], [20].

<sup>3</sup>The HARDIMAN I exoskeleton [25] attempted to do this as well, but with a flawed approach that neglected multi-joint coordination.

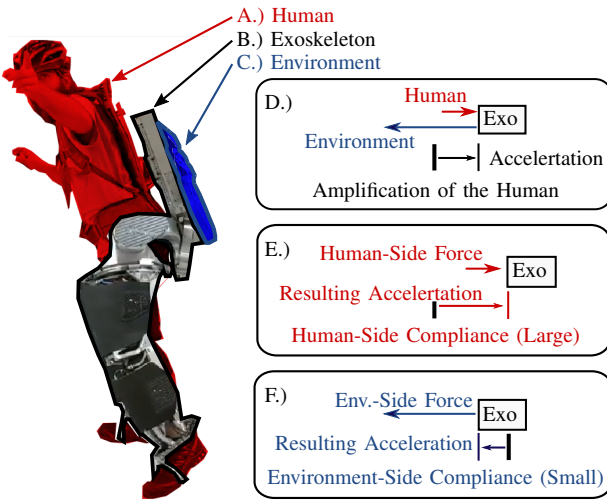


Fig. 1. Human–exoskeleton–environment interaction illustrating the concept of amplification. Marker A, the Human (inc. the backpack frame), connects to B, the Exoskeleton (the Apptronik Sagittarius), which connects to C, the Environment (an unknown load). The Human–Exoskeleton connection is force/torque sensitive. In D, E, and F a high-level schematic shows a mass-like exoskeleton (Exo) being acted on by forces to result in acceleration. In E and F the acceleration resulting from each force is shown, and D shows the total acceleration—the sum of the accelerations in E and F. Thanks to amplification control, the acceleration resulting from environment-side and human-side forces are *not equal*, and the human can overpower the environment even though the human-side force is smaller in magnitude than the environment-side force.

controller from [22] was still not designed to improve the human-side compliance relative to the torque-controlled gravity compensation strategy. It still used admittance control and a position-controlled robot. In this paper, we use force sensing at the human-robot and actuator-robot interfaces, and this serves the dual purposes of distinguishing the human from the environment and allowing torque control at the joints. The two interface compliances are then shaped with a cascade of amplification feedback on top of torque-controlled actuators.<sup>4</sup>

Unfortunately, the problem of non-passivity is inherent to feedback control that conceals inertia. This is an issue regardless of how the inertia was concealed—through positive acceleration feedback [13] or force feedback [28]. Without passivity, we must fall back to robust control in order to certify such behaviors. Most importantly, the exoskeleton’s human-facing port—its force–position relationship at the human–robot interface—will be in a feedback interconnection with the human’s robot-facing port. Studies of this feedback interconnection [29], [28], [30], [31] and the human in particular [32] have modeled the human as a mass-spring-damper system with a range of parameter values. The most variable parameter is stiffness, as this depends on muscle contraction [33]. We must demonstrate that no possible human behavior leads to instability—a robust control problem. Designing a machine to be passive [34], [35], [36], [37] can also be seen as a robust control problem: such designs guarantee stability against a very wide range of ‘human’ behaviors—the set of all passive

<sup>4</sup>More specifically, we use reaction force sensing series elastic actuators with torque control based on disturbance observers [26], [27].

transfer functions. Our prior work [38], [31], [32] has studied this stability problem for a table-mounted elbow exoskeleton.

In this paper, we scale up to a 12 degree of freedom (12-DOF) lower-body exoskeleton with 8 active and 4 passive joints. This includes a new multi-joint coordination approach modeled after humanoid robot controllers for torque-controlled joints [39], [40] (e.g. the Valkyrie robot at NASA JSC [41], [42]). More specifically, we contribute a comprehensive framework for achieving amplification control in exoskeletons that have torque-controlled joints and force sensing at the human interface. This contribution comprises (a) an optimization-based controller that determines robot joint torques using a prioritized list of ‘tasks’ and a set of constraints that act on the sum of human and robot torques—the ‘Shared-Body Controller’ (Sec. V); (b) a six degree of freedom (6-DOF) task that constrains the robot to follow human-led footstep transitions—the *inter-foot force task* (Sec. IV); (c) a frequency-domain amplification shaping control strategy that distills the complex approaches of [31] and [38] down to a single parameter tuning problem (Sec. III); (d) the construction of a generic amplification task that links the frequency domain control approach to the task-based framework (Sec. II); and (e) a demonstration of the control framework implemented in a lower-body exoskeleton (Sec. VI).

## II. THEORY OF STRENGTH AMPLIFICATION TASKS

Strength amplification can be illustrated using the example of an ideal fixed-base (arm-like) “exoskeleton” performing a force-feedback behavior with its human and environment contacting link (that is, its end-effector).

Consider a fully actuated, grounded base exoskeleton robot in contact with both a human operator (Jacobian  $J_c$ , and force  $f_c$ ) and an environment (Jacobian  $J_e$ , and force  $f_e$ ), using the notational system laid out in Tab. I,

$$M_e \ddot{q} + B_e + g_e = \tau + J_c^T f_c + J_e^T f_e, \quad (1)$$

where the environment and the human are acting as inputs to the system, and the joint torque vector  $\tau$  will be partially specified in terms of the measured human torque. We are interested in the way the human perceives the environment once the controller has been defined. We want to define a control that increases the magnitude of the human forces relative to the magnitude of the environmental forces within the context of, to borrow a concept from whole-body control for humanoids [39], a task.

Tasks describe behaviors we want the robot to achieve, for example moving an end effector to a desired pose in Cartesian space. The example task constrains 6-DOF, but it could also be divided into sub-components that preserve the DOF count, e.g. a 3-DOF position task and a 3-DOF orientation task. Tasks can also specify the desired internal forces of multi-contact [40]. More generally, tasks define both an effort-flow port of the robot and a target behavior for the robot to imitate at that port—a spring-damper behavior for position control and a force behavior for force control. This port is known as the task-space. By using the mapping between the joint-space of the robot and the task-space (and the mapping’s Jacobian,

TABLE I  
NOMENCLATURE FOR SEC. II

Symbol	Meaning
$M_e, B_e, g_e$	exoskeleton mass, Coriolis, gravity
$\ddot{q}, \dot{q}, q$	joint acceleration, velocity, position
$\tau$	joint torque vector
$J_c, f_c$	human interaction cuff Jacobian, forces
$J_e, f_e$	environment interaction Jacobian, forces
$J_t$	task Jacobian
$\bar{J}_t$	dynamically consistent pseudo-inverse of $J_t$
$x_t$	task position
$\hat{f}_t$	desired task force
$\alpha$	amplification rate

$J_t$ ), a whole-body controller can implement the task behaviors even while floating in zero gravity or maintaining contact with arbitrarily shaped ground [39].

An amplification task will also shape the behavior in its task-space. Assuming this task-space is acted upon by both a human (through a sensorized cuff) and an external force, the open-loop task-space dynamics can be written

$$\Lambda_t(\ddot{x}_t - \dot{J}_t \dot{q}) + \bar{J}_t^T(B_e + g_e) = \bar{J}_t^T(\tau + J_c^T f_c + J_e^T f_e), \quad (2)$$

where  $\Lambda_t = (J_t M_e^{-1} J_t^T)^{-1}$  is the task-space mass matrix and  $\bar{J}_t = M_e^{-1} J_t^T \Lambda_t$  is the dynamically consistent pseudo-inverse of the task Jacobian [40]. An amplification task will reshape these dynamics to the human's benefit by applying the following ideal task behavior:

$$\bar{J}_t^T \tau = (\alpha - 1) \bar{J}_t^T J_c^T f_c + \bar{J}_t^T(g_e), \quad (3)$$

where the first term represents amplification of the human operator's strength, and the second term compensates gravity. This controller yields the closed-loop task-space dynamics,

$$\Lambda_t(\ddot{x}_t - \dot{J}_t \dot{q}) + \bar{J}_t^T(B_e) = \alpha \bar{J}_t^T J_c^T f_c + \bar{J}_t^T J_e^T f_e. \quad (4)$$

These closed-loop dynamics amplify the influence of the human force by a factor of  $\alpha$ . But this behavior is complicated by the projection matrices  $\bar{J}_t^T J_c^T$  and  $\bar{J}_t^T J_e^T$ , which represent projection onto the space of the task as well as the potential for mismatch between the reference frames of the task, the cuff, and the external force.

To more clearly represent the special case where the human and environment forces act *only* in the task-space, let us assume, without loss of generality, that the human and environment forces are expressed in the units and reference frame of the task-space. For example, this is the case if: (1) both forces are applied to one sensorized, 6-DOF end effector; (2) the sensor measurements of the spatial force vectors of the human and the environment are all converted to the same reference frame [43]; and (3) this frame is also the frame in which the task is expressed. This special case leads to *ideal* amplification behavior.

**Definition 1** (Ideal Amplification Behavior). When the dynamics of a task are unchanged, except that the strength of the human is multiplied by a scalar  $\alpha > 1$ , as in

$$\Lambda_t(\ddot{x}_t - \dot{J}_t \dot{q}) + \bar{J}_t^T(B_e) = \alpha f_c + f_e, \quad (5)$$

we say the human is experiencing ideal amplification in the task-space.

This control gives the human a clear advantage, with respect to both environmental forces and the dynamics of the exoskeleton as perceived by the operator.

We can also express this advantage using a ratio of compliances. More specifically, we consider instantaneous compliances—transfer functions relating infinitesimal force to infinitesimal motion of the closed-loop robot. These instantaneous transfer functions change over time due to the non-constant mass matrix. But at any instant in time, the instantaneous compliance of the robot with respect to the human is *exactly*  $\alpha$  times its compliance with respect to the external force—because this simply restates the relationship between the coefficients on  $f_c$  and  $f_e$  in (5). Therefore, we can define amplification as the ratio of compliance transfer functions between the larger human-side compliance and the smaller environment-side compliance.

This concept of amplification matches that of [22] but describes it using robot dynamics free from a position controller. This highlights the backdrivable control foundation of our approach: the exoskeleton can be moved freely by the operator, and the amplification serves to mask some of the inertia and attenuate the external forces that an operator feels. The degrees of freedom in which this behavior occurs are controlled by the placement of the amplification tasks. Different degrees of freedom of the exoskeleton need not share an amplification rate (though this could distort the human perception of external forces). And the task definition mechanics allow these degrees of freedom to be expressed arbitrarily (not restricted, for example, to the joint-space of the robot or the operator).

We call this law ideal because it changes the apparent inertia the human feels instantaneously—which is quite a simplification. The law requires that the actuation bandwidth is infinite. Beyond the actuation bandwidth, all feedback systems asymptotically revert to their natural dynamics. Thus, in the high frequency asymptote, the two compliances should be equal; and their ratio, the amplification *transfer function*, should equal one. To design realizable amplification behaviors while satisfying these requirements, we will employ frequency domain tools.

### III. FREQUENCY DOMAIN AMPLIFICATION SHAPING

Since ideal amplification cannot be attained, we will need to consider the design space of realistic amplification behaviors. Frequency domain linear control theory offers the tools necessary to consider the stability and passivity of the various behaviors we could achieve via dynamically compensated force feedback.

#### A. Compliance Shaping

We will consider the way force feedback influences the mechanical impedance of the human–robot and human–environment ports. More specifically, we will study the compliance (integral admittance) of the exoskeleton at these two ports. This variant notation (compliance instead of impedance)

is helpful for considering the stability of a feedback interconnection with a spring.

Compliances are transfer functions representing position per force—expressing the same information as admittance or impedance which are velocity per force and force per velocity respectively. Shaping the amplification ratio without changing the backdrivable environment-side compliance is equivalent to shaping the human-side compliance. To help us in this endeavor we draw upon a set of Bode plot tools collectively known as the compliance shaping approach. These tools will allow us to design a compliance that will be stable when coupled to a simple model of the operator. This model lumps together the spring-like effects of the cuff structure, the operator’s biological soft tissue, and the operator’s musculoskeletal system.

Using force feedback control, we can achieve amplification that is a linear transfer function—despite the fact that both the human-side compliance and environment-side compliance are nonlinear, their ratio can be linear. However, to address stability questions in the frequency domain we must make conservative simplifications for both the human and the human-side compliance. In particular, we will make a useful simplification that the exoskeleton has some constant linear compliance that is dominated by inertial effects. Similarly, we will assume that the human has a constant linear compliance. These assumptions are useful in that they capture the primary failure mode of amplification systems: an oscillation between a mass-like exoskeleton and a spring-like human that gains energy due to the force feedback. But the assumptions, of course, fail to describe many other behaviors.

In addition to assuming linearity, we will further simplify by assuming that we can neglect the coupling between the three components of torque and the three components of force that exist between the human and the exoskeleton. This is useful in that it simplifies the stability analysis and avoids some very complex data-driven modeling problems. But it introduces some caveats, which we will discuss in Sec. VII-B.

The reason we use compliance transfer functions, and not admittance or impedance transfer functions, is to highlight the relationship between the system in parallel with a spring and the frequency domain design method for proportional feedback (as in [44] Chapter 6) [45], [38]. A compliance under proportional feedback has a controller with units of force per position—a spring stiffness. Thus, if we consider a compliance under proportional feedback using the Bode plot crossover point / phase margin technique to analyze stability, we are equivalently analyzing its stability with respect to linear springs. A more general phase margin concept could be applied to other representations of the system transfer function, but compliance plots stay closest to the textbook examples in that the feedback is proportional and the result is a low pass filter.

It is well established that energetic passivity of a port can be inferred from the phase of its transfer function representations. For admittance or impedance transfer functions, the system is passive if the transfer function is positive real. Since compliance is just admittance divided by  $s$ , the passive phase region shifts by  $-90^\circ$ . Thus, compliances are passive if their

TABLE II  
NOMENCLATURE FOR SEC. III

Symbol	Meaning
$C_H(s)$	c.l. human-side compliance
$H(s)$	human compliance
$K_h$	human stiffness
$\phi$	human phase lag
$M$	mass
$x(t), X(s)$	position
$f_E(t), F_E(s)$	environmental force
$f_A(t), F_A(s)$	actuation force
$F_H(t), F_H(s)$	human force
$\hat{\alpha}(s)$	desired amplification
$\alpha(s)$	realized amplification
$K(s)$	feedback controller
$C_E(s)$	environment-side compliance
$C_A(s)$	compliance w.r.t. actuation command
$\eta(s)$	actuation imperfections
$\lambda$	amplification bandwidth (tuning parameter)
$\alpha_0$	steady-state amplification rate
$\zeta$	amplification damping ratio

phase is in the range  $-180^\circ$  to  $0^\circ$ —the negative imaginary range.

The robot’s human-side interface is coupled to a system: a human wearing a physical cuff attachment. This system has many sources of flexibility: the physical cuff interface, the human’s soft tissue, and the human’s neuromuscular control—all of which are complicated and nonlinear. We model this whole system as an uncertain spring that pulls the physical cuff interface towards the human’s desired equilibrium. This desired equilibrium can change when the human intends to move dynamically, but the transfer function is with respect to this equilibrium point, so it is still valid. This spring is “the human” for the purposes of controller design.

The spring-type model allows us to check for stability using the *phase margin* of human-side compliance for every crossover within the stiffness range. While this model neglects inertia, this neglect will only make the model more conservative when we use it later. The model also appears to neglect any dissipation or damping effects, but this is *not* the case. We represent dissipation by making stiffness a *complex number*.

As demonstrated in the human elbow joint [32], the complex stiffness model is not just a mathematically convenient model, but also a more accurate description of real human-in-exoskeleton behavior than the linear spring-damper. The complex stiffness model results in a human compliance transfer function with a constant magnitude and a constant phase-lag. And this phase lag represents the non-linear damping properties of the human. The model is explicitly only a frequency domain model, but the behavior is similar to what might be achieved with hysteresis or coulomb friction.

Because our human model includes some energy-dissipating phase lag, it is easier to achieve coupled stability with humans than with an ideal spring. To represent this distinction, we introduce the ‘Human Phase Margin.’

**Definition 2.** A compliance  $C_H(s)$  in parallel with a complex human compliance  $H(s) = K_h^{-1}e^{\frac{\pi}{180}\phi j}$  with phase lag  $\phi$ ,  $-90^\circ < \phi < 0$ , which intersects at a “human crossover frequency”  $\omega$  such that  $\|H(j\omega)\| = \|C_H(j\omega)\|$  has a “human

phase margin" equal to  $\angle C_H(j\omega) - \phi + 180^\circ$ .

Rather than comparing compliance phase  $\angle C(j\omega)$  to a  $-180^\circ$  reference, as in the traditional phase margin, the human phase margin compares it to a  $\phi - 180^\circ$  reference, where  $\phi$  is the phase lag of the human's complex spring. This concept is closely related to the phase-based passivity relaxations in [38], [45] in that systems which are relaxed-phase passive within  $\phi$  are stable in interconnection with this human model.

This human phase lag is an imminently exploitable phenomenon in amplification controller design, as the 'Human Phase Margin' criterion is easier to satisfy than the traditional one. Our controller exploits this assumption by having a human-side compliance that asymptotically approaches  $-180^\circ$  from below. Note that this means that there exist ideal springs which, in parallel with the human-side compliance, would destabilize the exoskeleton. But for humans above a minimum stiffness and phase lag magnitude, this human-side compliance is still safe.

The human phase margin also explains our omission of inertia from the human model. This inertia would also drop the human compliance phase and would improve the human phase margin (mostly at higher frequencies than our controller bandwidth). Thus, ignoring it does not hurt us—it just makes the stability condition more conservative, particularly at high frequencies.

### B. Compliance Shaping for Strength Amplification

Fig. 2 shows a progression of block diagrams and four Bode plots that describe the frequency domain model of the system as well as the construction of the controller (in notation following Tab. II).

Fig. 2.A shows the one-dimensional representative time domain free body diagram, where the exoskeleton acts like an inertia and is being acted upon by three forces: the human  $f_H(t)$ , the actuator  $f_A(t)$ , and the environment  $f_E(t)$ . We could describe it,

$$M\ddot{x}(t) = f_E(t) + f_H(t) + f_A(t), \quad (6)$$

where  $M$  is the mass of the exoskeleton and  $x(t)$  is its position.

We then take this into the frequency domain with Fig. 2.B, where the Laplace transform of the exoskeleton's position,  $X(s)$ , is the sum of three inputs ( $F_E(s)$ ,  $F_H(s)$ , and  $F_A(s)$  being the Laplace transforms of the environmental force, the human force, and the actuator force respectively) weighted by compliance transfer functions. The compliance of the exoskeleton,  $C_E(s)$  is simply the compliance of the exoskeleton inertia:

$$C_E(s) = \frac{1}{Ms^2}. \quad (7)$$

The compliance with respect to actuation forces,  $C_A(s)$ , introduces some imperfections which we model as the transfer function  $\eta(s)$ :

$$C_A(s) = C_E(s)\eta(s). \quad (8)$$

These imperfections include a low pass filter restricting the bandwidth of the actuation, and a time delay. (A comparison

between  $C_E(s)$  and  $C_A(s)$  is shown in the Bode plot of Fig. 2.H.)

The next block diagram (Fig. 2.C) introduces the controller as a transfer function  $K(s)$ . This ultimately produces a new human-side compliance  $C_H(s)$ , as shown in Fig. 2.D. Our controller structures  $K(s)$  according to a desired closed-loop amplification behavior  $\hat{\alpha}(s)$  (not to be confused with the realized amplification behavior  $\alpha(s)$ ). We define the realized amplification as

$$\alpha(s) = \frac{C_H(s)}{C_E(s)} = 1 + \eta(s)K(s), \quad (9)$$

and the desired amplification,  $\hat{\alpha}(s)$ , is an approximation of this value that neglects the controller imperfections represented in  $\eta(s)$ , that is

$$\hat{\alpha}(s) = \frac{C_E(s) + K(s)C_E(s)}{C_E(s)} \quad (10)$$

$$= 1 + K(s). \quad (11)$$

### C. Second Order Lag Amplification Shape

We parameterize this desired amplification transfer function as a second order lag, with two conjugate poles at lower frequency than two conjugate zeros.

$$\hat{\alpha}(s) = \frac{s^2 + 2\zeta\omega_z s + \omega_z^2}{s^2 + 2\zeta\omega_p s + \omega_p^2}, \quad (12)$$

using the same  $\zeta$  twice for convenience, though this could potentially be optimized. While this  $\hat{\alpha}(s)$  is not strictly causal, it produces a  $K(s)$  which is:

$$K(s) = \hat{\alpha}(s) - 1 = \frac{2\zeta(\omega_z - \omega_p)s + \omega_z^2 - \omega_p^2}{s^2 + 2\zeta\omega_p s + \omega_p^2}. \quad (13)$$

This controller is compared to an example of realized  $\alpha(s)$  in Fig. 2.I's Bode plot.

The realized behavior can be understood from the Bode plot in Fig. 2.J, which compares the environment-side compliance  $C_E(s)$  with the human-side compliance  $C_H(s)$ . The human-side compliance has been increased at low frequencies to reach an asymptotic magnification of the environment-side compliance at low frequencies. Also plotted is a representative human compliance,  $H(s)$ . Following the work of [32], this is modeled as a complex stiffness. That is, the human behaves like a spring with a constant phase lag at all frequencies<sup>5</sup> (suspected to be from hysteretic joint friction). Stability of the human-side compliance when coupled to this human compliance is the key limiting factor on the amplification bandwidth. This will be discussed more with Fig. 3.

### D. The Environmental Port

A human compliance in parallel with the closed-loop exoskeleton produces a feedback system shown in Fig. 2.E. Closing this loop produces a single input transfer function

<sup>5</sup>For all frequencies below the human's own natural frequency, which is much higher than that of the exoskeleton for our purposes.

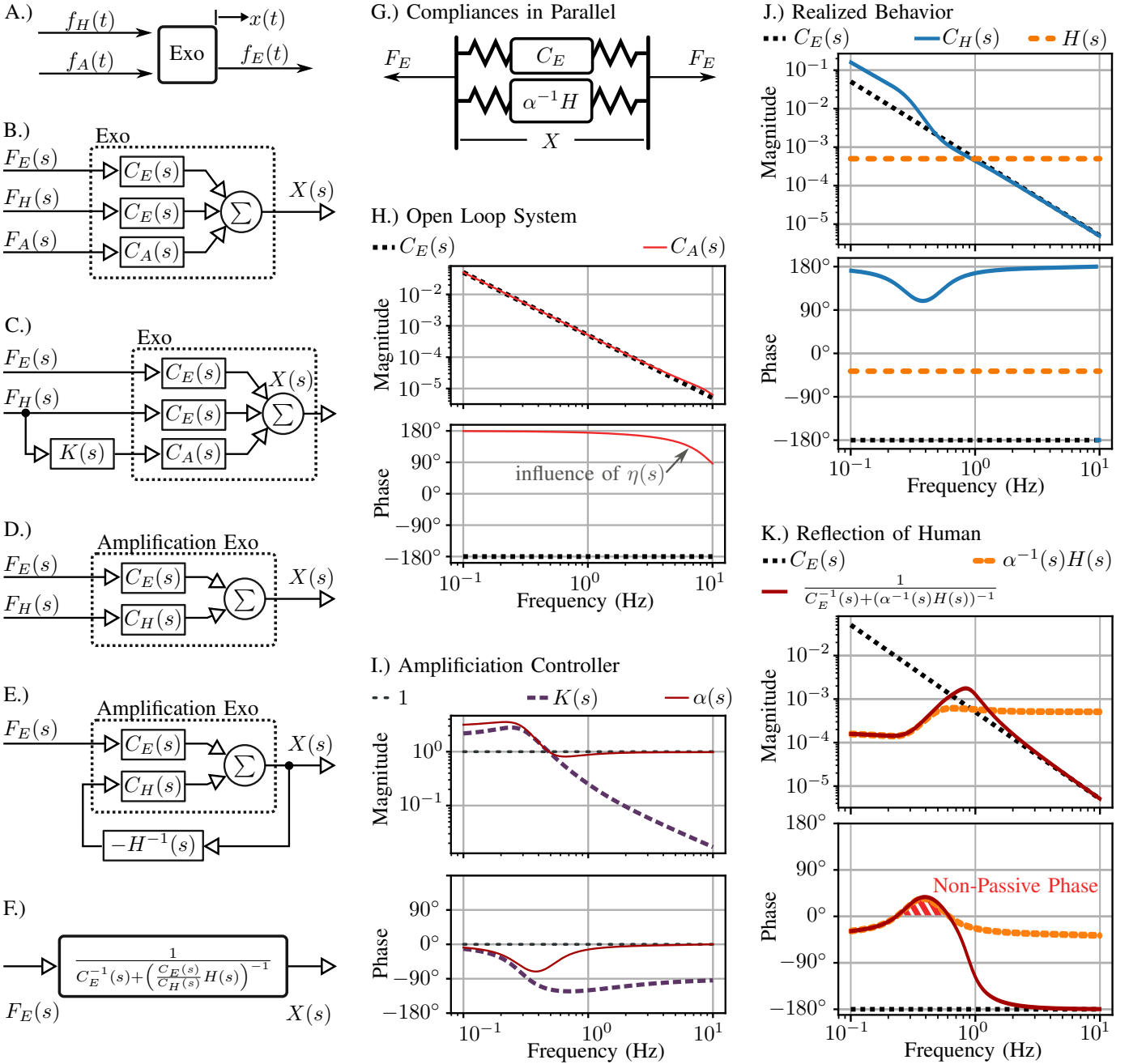


Fig. 2. Block diagrams and Bode plots explaining the controller. A.) Three forces acting on the inertia of the exoskeleton in a one dimensional model. B.) This model represented as a block diagram with three inputs and one output. C.) The addition of amplification control (controller  $K(s)$ ) to the exoskeleton system. D.) The resulting closed-loop system has only two inputs. E.) The interconnection of the closed-loop amplification exoskeleton with a human stiffness (human compliance  $H(s)$ ). F.) The resulting one-input block diagram. G.) An equivalent representation as the parallel interconnection of two compliances:  $C_E(s)$  — the compliance of the exoskeleton with respect to external forces, and  $\alpha^{-1}H(s)$  — the compliance of the human reflected through the amplification effect (amplification rate  $\alpha(s)$ ). H.) A Bode plot of the open loop system, showing mass-like behavior for the exoskeleton, and some phase lag from time delay and low-level control for the actuator-side compliance. I.) A Bode plot of the controller itself.  $K(s)$  is designed as  $\alpha(s) - 1$  for some desired  $\alpha(s)$ . J.) A bode plot of the closed-loop behavior of the amplification exoskeleton, with the human compliance,  $H(s)$ , for reference. The human compliance is significant when tuning  $\alpha(s)$ . K.) Amplification alters the human behavior as it appears for the environment, making the human stronger but altering the phase. The resulting behavior is not necessarily passive, as shown by its phase.

representing the only remaining input, the environmental force  $F_E(s)$ , determining the position  $X(s)$ :

$$\frac{X(s)}{F_E(s)} = \frac{1}{C_E^{-1}(s) + \left(\frac{C_H(s)}{C_E(s)}H(s)\right)^{-1}}, \quad (14)$$

which we write here as a harmonic sum of the two compliances  $C_E(s)$  and  $\alpha^{-1}(s)H(s)$ . This harmonic sum construction can be visualized as these two compliances being interconnected in parallel, as shown in Fig. 2.G.

These two compliances, as well as the total compliance of  $X(s)/F_E(s)$ , are shown in Fig. 2.K. They illustrate that the

application of the inverse amplification rate to the spring-like human compliance reflects it to the environment in a way that is not passive, as we can observe using its phase. This non-passivity is restricted to the mass-type, and the system is potentially destabilized if the human in the exoskeleton tries to move objects that are slightly more massive than the exoskeleton itself (such that the Bode magnitude plot of the offending inertia intersects the total compliance at a frequency corresponding to a non-passive phase). In terms of interacting with spring-like environments, however, the system should work well—and this includes such high-stiffness environments as the ground.

It seems possible that this non-passivity could be avoided if the bandwidth of the amplification were much higher, as in this case the inertia of the exoskeleton could “hide” the non-passivity of the reflected operator. This is hard to do, unfortunately, since the poles of  $\hat{\alpha}(s)$  would need to occur at a frequency higher than that of the Bode magnitude plot intersection of  $H(s)$  and  $C_E(s)$ . This brings us to an important point about the minimum-phase property of the zeros of  $\alpha(s)$ : these zeros are only minimum phase so long as the phase of  $K(s)\eta(s)$  at the point where its magnitude equals unity has not dipped below  $-180^\circ$ . The phase lag of  $\eta(s)$  only drops with frequency, so this acts as a limit on the amplification’s bandwidth. To go beyond the natural man-machine resonance would require carefully designed high bandwidth actuation, or operators acting uncharacteristically softly, even when surprised—which seems counter to their instincts. Bandwidth limits and operator safety concerns kept us from attempting this type of control on the real robot.

### E. One Parameter Tuning Strategy

Accepting this non-passivity, what remains is to tune the controller to drop the amplification magnitude to the left of the  $C_E(s)$ - $H(s)$  crossover without making the human–robot system unstable. To facilitate easy tuning of our controller we introduce one parameter  $\lambda$ , the amplification bandwidth (equal to  $\omega_p$  which we tune, and a low frequency amplification gain  $\alpha_0 \geq 1$  (equal to  $\omega_z^2/\omega_p^2$ ), so that

$$K(s) = \frac{2\zeta(\sqrt{\alpha_0} - 1)\lambda s + (\alpha_0 - 1)\lambda^2}{s^2 + 2\zeta\lambda s + \lambda^2}. \quad (15)$$

Our controller can be tuned without knowing the exoskeleton inertia, human stiffness, or even the human phase lag since  $\lambda$  is the only tuning parameter, the system is stable for infinitesimal  $\lambda$ , and the human phase margin decreases as  $\lambda$  increases.

Fig. 3 marks the point at which the total human-side compliance of the exoskeleton intersects a human compliance in the Bode magnitude plot as the crossover point. This frequency of intersection is the human crossover frequency, and the phase of the human-side compliance of the exoskeleton is compared to  $-180^\circ + \phi$ , where  $\phi < 0$  is the phase lag of the human compliance. This human phase margin determines whether the closed-loop system will have a pole in the right half plane, as can be observed from its phase behavior in the Bode plot in Fig. 3. With higher pole frequencies the pole-pair’s phase transition becomes more and more abrupt (like that of a perfect

oscillator) and eventually becomes unstable—the increasing phase with frequency being a tell-tale indicator of a right half plane pole-pair.

A single tuning experiment can determine the limiting bandwidth for any particular amplification shape. Starting with  $\lambda$  very low, we slowly scale it up until the system appears to vibrate. Once the threshold of oscillation is found, the oscillation frequency is roughly the crossover frequency, and we could obtain an estimate of the human phase if we had a good model of the torque tracking performance and time delay. The problem is practically solved, however, by the formulation of the controller in a one-parameter tunable way. With one knob, it is easy to increase the performance up to the limit, back off for robustness, and get a good result in the end.

### F. As a Whole-Body Control Task

In this way, we can easily define the 6-DOF *amplification task* of the robot’s hip/backpack link in the reference frame of the hip, as a combination of 6 *amplification task* sub-components for each element of the spatial force vector. For the  $i^{\text{th}}$  *amplification task* sub-component, we can write the desired task force  $f_{a,i}^d$  according to the a (cuff) sensor force in that task dimension  $f_{c,i}$ ,

$$f_{a,i}^d(s) = K_i(s)f_{c,i}(s), \quad (16)$$

where  $K_i(s)$  is potentially different for each independent *amplification task* sub-component. We combine all the *amplification task* sub-components together into a 6-vector

$$f_a^d(s) = \mathbf{K}(s)f_c(s), \quad (17)$$

where  $\mathbf{K}(s)$  is a diagonal matrix of all the amplification filters,  $f_c(s)$  is the 6-axis force/torque sensor measurement (converted to the hip frame), and  $f_a^d(s)$  is the desired *amplification task* spatial force vector. This vector is the output of the amplification filtering module and is treated as the time-domain vector signal  $f_a^d(t)$  in Sec. V.

## IV. INTER-FOOT FORCE TASK

Human-led foot contact transitions, such as walking or shifting balance, are an important part of any scheme for controlling lower-body exoskeletons, and they do not naturally emerge from the *amplification task* as one might hope. To allow this critical feature we introduce a second task, the *inter-foot force task*, that is achieved simultaneously and causes the exoskeleton to follow human-initiated foot lifting.

With one foot on the ground, this foot acts as a virtual base for the exoskeleton—a contact constraint on its otherwise free-fall dynamics. Since the exoskeleton is not designed to jump, we can assume that some sort of virtual base always exists. When two feet are on the ground at the same time, we can imagine a virtual single foot between them that acts like a base and moves between the feet according to the operator’s own weight distribution.

Two feet together have 12-DOF worth of reaction forces, and the virtual single foot contact only allows 6-DOF to be used as a virtual base. The remaining 6-DOF can be thought of as an error, representing the mismatch between the 12-DOF

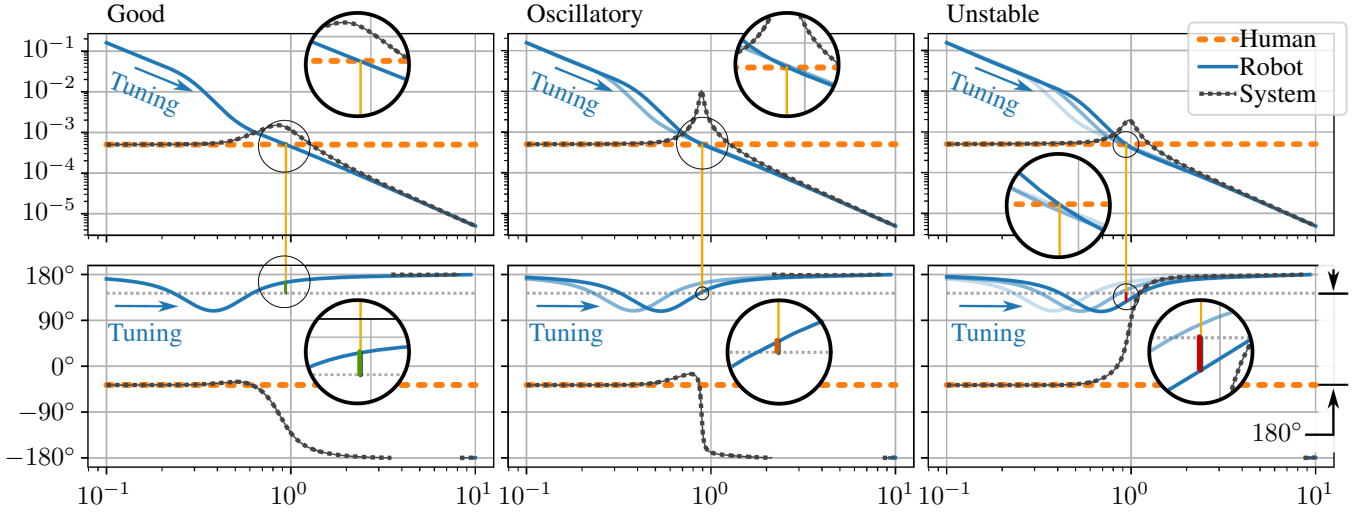


Fig. 3. One parameter tuning of the amplification filter. Three bode plots show three different tuning configurations as the single tuning parameter (the amplification bandwidth  $\lambda$ ) is increased to failure. Tuning arrows indicate increasing  $\lambda$ . Plotted are the compliance of the human (Human), the human-side compliance of the robot (Robot), and the compliance of the two when interconnected in parallel (System). In all three bode plots, magnification is used to highlight the calculation of the “Human Phase Margin.” This calculation uses the phase of (Robot) at the frequency where the magnitude of (Robot) is equal to the magnitude of (Human)—the crossover frequency. At this frequency, stability of the resulting human–robot interconnection is determined by comparing the phase of (Robot) to a reference phase  $180^\circ$  offset from the phase of (Human). The difference between the phase of (Robot) and this reference is the “Human Phase Margin.”

TABLE III  
NOMENCLATURE FOR SEC. IV

Symbol	Meaning
$f_i$	foot $i$ 's spatial force vector in frame $i \in \{1, 2\}$
$f$	stacking of $f_1$ and $f_2$
$f_s$	sum of foot spatial force vectors in frame $s$
$Q_1, Q_2, Q$	reaction force cost definition matrices
${}^b X_a^*$	spatial force vector transform, frame $a \rightarrow$ frame $b$
$\lambda$	Lagrange multiplier vector in optimization
$X$	equality constraint matrix in optimization
$\Gamma = [XQ^{-1}X^T]^{-1}$	
$\bar{X} = Q^{-1}X^T\Gamma$ , a pseudo-inverse of $X$	
$f_d$	inter-foot force task error in frame $d$
$\bar{X}$	weighted inter-foot difference matrix
$\mathbf{G}$	virtual base definition matrix

space of reaction forces, and the 6-DOF space of reaction forces that agree with the virtual single foot contact model. This error should be zero, and eliminating it is the purpose of the *inter-foot force task*.

We define a virtual single foot contact for the robot indirectly by defining the way that the net reaction force would be split into two components, one for each foot. This splitting is accomplished with the following equality constrained quadratic programming problem.

$$\underset{f_1, f_2}{\text{minimize}} \quad \frac{f_1^T Q_1 f_1}{2} + \frac{f_2^T Q_2 f_2}{2} \quad (18)$$

$$\text{subject to} \quad {}^s X_1^* f_1 + {}^s X_2^* f_2 = f_s, \quad (19)$$

where  $Q_1$  and  $Q_2$  are positive definite and typically diagonal. We introduce two new reference frames: frame  $s$  (for “sum”), and frame  $d$  (for “difference”). Both frames are weighted averages of the two foot frames. Frame  $s$  is approximately matched with the human center of pressure. Frame  $d$  is the

mirror image of frame  $s$ , and both frames overlap at the mid-foot point when the human puts equal weight on each foot. Transformation  ${}^s X_1^*$  converts spatial force vectors from the 1<sup>st</sup> foot's frame to frame  $s$ , and  ${}^s X_2^*$  is the same for the other foot. The force  $f_s$  represents the sum of the two foot spatial force vectors expressed in frame  $s$  (Tab. III).

The equality constrained quadratic programming problem can be solved analytically. Starting from the equilibrium conditions,

$$\underbrace{\begin{pmatrix} Q_1 \\ Q_2 \end{pmatrix}}_Q \begin{pmatrix} f_1 \\ f_2 \end{pmatrix} + \underbrace{\begin{pmatrix} {}^s X_1^* & {}^s X_2^* \end{pmatrix}}_X^T \lambda = 0, \quad (20)$$

$$X f = f_s. \quad (21)$$

In matrix form,

$$\begin{pmatrix} Q & X^T \\ X & 0 \end{pmatrix} \begin{pmatrix} f \\ \lambda \end{pmatrix} = \begin{pmatrix} 0 \\ f_s \end{pmatrix}, \quad (22)$$

$$\begin{pmatrix} f \\ \lambda \end{pmatrix} = \begin{pmatrix} Q^{-1} - \bar{X} X Q^{-1} & \bar{X} \\ \bar{X}^T & -\Gamma \end{pmatrix} \begin{pmatrix} 0 \\ f_s \end{pmatrix}, \quad (23)$$

where  $\Gamma = [XQ^{-1}X^T]^{-1}$  and  $\bar{X} = Q^{-1}X^T\Gamma$ . Thus

$$f = (Q^{-1}X^T) \cdot [XQ^{-1}X^T]^{-1} f_s, \quad (24)$$

$$\begin{pmatrix} f_1 \\ f_2 \end{pmatrix} = \begin{pmatrix} Q_1^{-1} {}^s X_1^{*T} \\ Q_2^{-1} {}^s X_2^{*T} \end{pmatrix} \cdot [{}^s X_1^* Q_1^{-1} {}^s X_1^{*T} + {}^s X_2^* Q_2^{-1} {}^s X_2^{*T}]^{-1} f_s. \quad (25)$$

This 12-DOF solution  $f$  is the virtual single foot contact's distribution of reaction forces between the two feet. The other six degrees of freedom in the foot forces—the degrees of freedom not specified by constraint (19)—represent the *inter-foot force task* error. More specifically, we define the *inter-foot*

force task error  $f_d$  in frame  $d$  to complete a parameterization of the foot forces  $f$

$$f = \bar{X} f_s + [I - \bar{X}(\bar{X}^T \bar{X})^{-1} \bar{X}^T] \tilde{X}^T f_d, \quad (26)$$

where we introduce

$$\tilde{X} = \begin{pmatrix} {}^d X_1^{-*} w_2 \\ - {}^d X_2^{-*} w_1 \end{pmatrix}, \quad (27)$$

as a rough parameterization of the deviation from the desired force distribution. This gets contorted into being perpendicular to  $\bar{X}$  by the pre-multiplication with an  $\bar{X}$  image space nullifier. Ultimately, the *inter-foot force task* tries to eliminate  $\|f_d\|$ , and when it is completely eliminated the reaction forces minimize the previously defined quadratic cost (since  $f = \bar{X} f_s$ ). This leaves  $f_s$  as the path of least resistance the optimization uses to hold up the weight of the robot.

We define  $\mathbf{G}$  to simplify notation:

$$f = \mathbf{G} \cdot \begin{pmatrix} f_s \\ f_d \end{pmatrix}, \quad (28)$$

$$\mathbf{G} = (\bar{X} \quad [I - \bar{X}(\bar{X}^T \bar{X})^{-1} \bar{X}^T] \tilde{X}^T). \quad (29)$$

#### Interpreting the Controller Through Reaction Forces:

As mentioned in Sec. I, our exoskeleton controller is tasked with simultaneously accomplishing the *amplification task* at the hip/backpack interface (Sec. III) and the *inter-foot force task*. In terms of reaction forces, the *amplification task* serves a similar purpose to the centroidal momentum task introduced in [46] or the center of mass task in [39]: it determines the required sum of reaction forces. Meanwhile, the *inter-foot force task* (similar to the internal force tasks from [40]) determines the part of the reaction force vector that is decoupled from the center of mass acceleration. With both tasks active, the reaction forces are all defined and the joint torques can be thought of as resulting from an inverse dynamics process—as in the Dynamic Balance Force Control of [47].

## V. WEIGHTED 1-NORM SHARED-BODY CONTROL

To combine the *amplification task* and *inter-foot force task* while also respecting limitations on the exoskeleton, we compute the joint torques of the exoskeleton using a linear optimization problem. This problem uses concepts of contact constraints, prioritization between task sub-components, a weighted 1-norm cost, and the actuator-mapped reaction force space in order to be computationally efficient.

### A. Contact Constraints

There is an important caveat to this concept of a virtual single-foot contact. Unlike actual fixed-base robots, robots with feet can topple over. Since an exoskeleton is essentially a humanoid robot (in feedback interconnection with a human), the inequality-constrained floating base models [46], [40], [48] are still relevant to keeping its feet flat on the ground. These constraints act on the base-ground reaction forces,  $f_r$ , which are not part of the standard *fixed-base* robot model. They are

TABLE IV  
NOMENCLATURE FOR SEC. V

Symbol	Meaning
$\tau$	optimization variable: joint torque vector
$M_e, B_e, g_e$	exoskeleton mass, Coriolis, gravity
$\ddot{q}, \dot{q}, q$	joint acceleration, velocity, position
$S$	underactuation matrix for a free floating base
$J_c, f_c$	Jacobian for human contact and forces
$J_r, f_r$	Jacobian for ground contact and (reaction) forces
$C_r, c_r$	foot contact inequality matrix and bias
$e(\cdot)$	a task error function
$\sigma(\cdot)$	a task scalarization function
$s_+, s_-$	1-norm slack variables
$w$	weight vector
$J_a, f_a, \dot{x}_a$	Jacobian, force, accel. for the <i>amplification task</i>
$J_f, f_f, \dot{x}_f$	Jacobian, force, accel. for feet
$\mathbf{J}, \mathbf{f}, \dot{\mathbf{x}}$	Jacobian, force, accel. for composite task
$\bar{\mathbf{J}}$	Dynamically consistent pseudo-inverse of $\mathbf{J}$
$\Lambda$	inertia matrix in composite task frame
$\mathbf{G}$	virtual base definition matrix
$\bar{\tau}$	maximum torque, human + exoskeleton
$f_d^a$	vector of desired <i>amplification task</i> forces

defined by the combination of a *floating-base* model and a contact constraint:

$$M_e \ddot{q} + B_e + g_e = S \tau + J_c^T f_c + J_r^T f_r, \quad (30)$$

$$J_r \ddot{q} + \dot{J}_r \dot{q} = 0, \quad (31)$$

with notation as in Tab. IV. To avoid tilting the feet, sliding the feet, or pulling on the ground, additional inequality constraints must be maintained,

$$C_r f_r + c_r \geq 0. \quad (32)$$

The inequalities described by  $C_r$  and  $c_r$  are simple approximations of the friction cone: for example, two rows would be used to express  $\mu |f_x| \leq f_z$ , where  $\mu$  is the friction coefficient. But the size of  $C_r$  depends on how many feet are on the ground. In addition to these limits due to contact, there are upper bounds to the torque magnitude the robot can provide. And if some of the joints are not actuated, then they have an upper limit of zero. These inequalities, when active, prevent the simultaneous satisfaction of all the robot's goals. This presents a clear problem for the *Shared-Body Controller*: how should the robot behave when the inequalities constrain the robot's ability to satisfy its tasks?

Our approach to this problem is to prioritize the *task sub-components*. And then, because a strict prioritization is not computationally feasible for our hardware, we approximate the lexicographic optimization with a 1-norm cost. Additionally, we reduce the size of the optimization problem by representing all reaction forces in terms of joint torque.

### B. Prioritized Tasks

With multiple tasks and inequality constraints, the robot's behavior is often over-specified. For example, the combination of the lateral (y-axis force) component of the *amplification task*, the mediolateral-plane rotation (x-axis torque) component of the *amplification task*, and the stance-foot's lateral center-of-pressure limitation may require a non-zero task error. This is easy to visualize if the robot's hip is far from the stance foot:

the ground reaction force can point toward the hip and avoid rotation, or it can point straight up and avoid lateral force, but it cannot do both simultaneously. A more general version of this problem is well known in the humanoid robotics community [49]. This happens frequently during dynamic walking. And it demands that we specify not only which tasks we want to achieve, but in which order the task sub-components should fail to be satisfied if they conflict in this way.<sup>6</sup>

When constraints become active, there is neither an obvious choice for what to give up nor an analytical method to optimally decide. However, if we provide a *prioritization* of the task sub-components, then an optimal answer exists. This prioritization requires additional parameters—a rank order for each task sub-component—but these are relatively few, and easy to understand and adjust. This approach has also been used to handle redundancy in task definition even without the limitation of constraints [39]. When constraints become active, the prioritization approach simply abandons the task sub-components one at a time, starting with the least important, until the problem is solvable. The lowest priority task sub-components are the ones for which we feel the human will have the easiest time comfortably handling the task sub-component failure. In the case of our *amplification task*, this could mean a failure to amplify the interaction force and/or a failure to achieve gravity compensation. In the case of our *inter-foot force task*, it could mean applying a force to the user's swing foot (failure to gravity compensate) or failing to match the user's desired contact force distribution (failure to transition appropriately, most evident if a foot is load-bearing when it should not be).

Strict prioritization between the tasks is a mathematically well-defined optimization scheme known as lexicographic optimization [50]. Lexicographic problems must be solved as a series of related optimization sub-problems. First, the most important cost must be optimized within the problem constraints—the first optimization sub-problem. Next, the second most important cost must be optimized within both the original problem constraints and a new constraint. This new constraint requires that the previously minimized cost for the most important objective stays at its previously determined optimal value. With a solution to this second optimization sub-problem, a lexicographic optimization would proceed forward one cost at a time, solving optimization sub-problems with an ever-increasing list of constraints. And this recursive process will continue until each component of the prioritized list of costs has been optimized in its own sub-problem. In our hardware, we could only solve three lexicographic optimization sub-problems within our one millisecond real-time control window, so with 12 prioritized task sub-components, a proper lexicographic solution was outside the realm of plausibility.

### C. Weighted 1-Norm Cost

Ref. [50] shows that weighted scalarization costs can approximate a lexicographic optimization in the context of

<sup>6</sup>After trying both prioritizations, we determined that the operator prefers a failure in x-axis torque balance, even if this causes the exoskeleton's hip to “wobble” relative to the human's with every step due to the compliance of the backpack attachment in this degree of freedom.

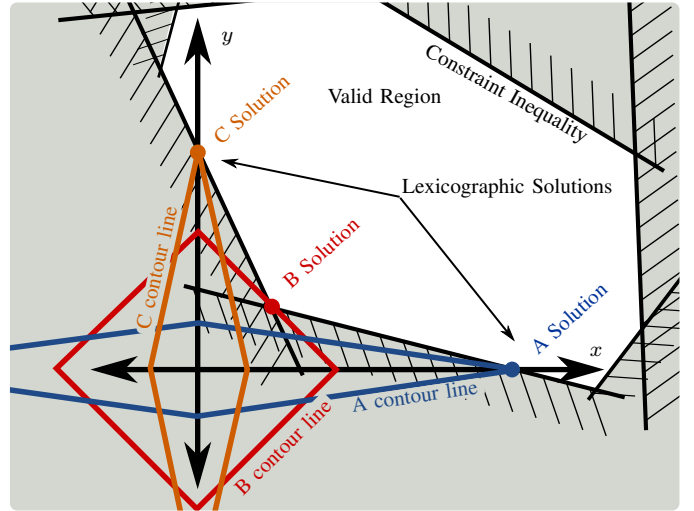


Fig. 4. Illustration of how weighted 1-norm costs can behave similarly to lexicographic (prioritized) costs. Plot in the space of task error for task- $x$  and task- $y$ . Weighted 1-norm costs A, B, and C are depicted with a single contour line each. Optimal solutions for each task shown as colored circles. The so-called “sparsity promoting” nature of the weighted 1-norm cost can be understood in this context as optimal solutions which sacrifice one task to achieve the other. As exemplified by cost B, however, this is not guaranteed and depends on the inequality constraints and the shape of the valid region they generate.

humanoid control. We used a scalarization that retains the linearity of the cost function, but we added two positive slack variables and two inequality constraints for each scalarized cost (which were all task elements) in order to do so. For our vector of task errors  $e(\tau)$  (expressed as a function of torque, as will be elaborated on in Sec. V-D), we define a vector of scalarizations  $\sigma(\tau)$

$$\sigma(\tau) = s_+ + s_- \quad (33)$$

where

$$s_+ \geq e(\tau), \quad \text{and} \quad s_- \geq -e(\tau), \quad (34)$$

where  $s_+$ , and  $s_-$  are the newly introduced vector slack variables, and the new vector inequalities in (34) are elementwise inequalities. Under conditions that are almost always met,<sup>7</sup>  $\sigma(\tau) = |e(\tau)|$  (as an elementwise absolute value).

This approach to modelling an absolute value function within the confines of a linear programming problem is the key to our application of a weighted 1-norm cost on the vector of all task errors. Clearly, summing the elements of  $\sigma(\tau)$  results in the vector 1-norm of  $e(\tau)$ . Summing the elements of  $\sigma(\tau)$  with positive weightings (setting cost equal to  $w^T \sigma(\tau)$  for some vector of positive weights  $w$ ) is a weighted scalarization in the sense of [50], but we can also think of it as a weighted 1-norm—as the 1-norm for a scaled version of the original space. We prefer this as a name for the way it invokes a lozenge-like rhomboid geometry in 2D, and a diagonally-scaled octahedron geometry in 3D.

To capitalize on this 2D intuition, Fig. 4 illustrates how the weighted 1-norm cost can be adjusted through the weighting

<sup>7</sup>Specifically that each element of  $\sigma(\tau)$  appears in the cost with a strictly positive weight, and that  $\sigma(\tau)$ ,  $s_-$ , and  $s_+$  are otherwise decoupled from the problem.

to approximate different lexicographic costs (there are only two in 2D space: either  $x$  matters more than  $y$  or vice versa). The illustration features a convex 2D set of solutions which satisfy constraints. The two axes represent orthogonal tasks, with the origin representing zero error for both tasks. Cost A uses a weighting that penalizes  $y$  error more than the  $x$ , cost B penalizes them roughly equally, and cost C penalizes  $x$  error more than  $y$ . In both cases A and C, the minimum cost point which satisfies constraints falls on one of the two axes—exactly as a lexicographic solution would. The fact that 1-norm costs tend to produce solution vectors with many zero entries (so-called “sparse” solutions [51]) is well known and frequently exploited. To promote *lexicographic solutions* instead of simply solutions with many zeros requires tuning the penalty weights to favor the prioritized tasks. In our illustration, the weightings in A and C are sufficiently extreme, and two lexicographic solutions emerge. Cost B illustrates a non-lexicographic middle-ground: neither cost is penalized enough to completely dominate the other, and the solution vector assigns non-zero error to both tasks.

One disadvantage of weighted 1-norm costs in robot control is that the constraints are continuously varying due to the changing robot geometry, and this can cause the optimal behavior to jump discontinuously. This can occur if the 1-norm cost discontinuously switches from being aligned with one lexicographic solution to a different lexicographic solution or even a non-lexicographic solution. We call these abrupt switches “priority inversion events.” To avoid these events entirely, we would need 1-norm weights with near-infinite scale differences between task sub-components. Since this is obviously not possible with floating-point numbers, the weighted 1-norm is an approximation: it sacrifices accuracy for speed. Fortunately, the approximation of the lexicographic problem is asymptotically perfect as the weight discrepancy increases, and the numerical precision of the linear program solver allowed us sufficient space to set these weights orders of magnitude apart and achieve reliable reproduction of the lexicographic problem in practice.

#### D. Actuator-Mapped Reaction Force Space

In order to speed up the solver and increase its accuracy, we reduce the number of free variables in our optimization problem by handling some equality constraints in advance. This is not necessary theoretically, as the problem is not actually changed by handling these constraints, however attempts to lean on the solver’s own ability to perform linear algebra resulted in disappointing precision and speed. Thus, we found the need to quickly re-express reaction forces as functions of joint torque.

More specifically, we find  $(f_a(\tau)^T, f_f(\tau)^T)^T$ —the mapping from the 12-DOF joint torque vector to an 18-DOF vector of forces that concatenates the ground reaction forces with the human–robot interaction forces at the backpack.<sup>8</sup> We

<sup>8</sup>Ultimately we only care about the 12-DOF vector of the *inter-foot force task* error and *amplification task* error,  $(f_a(\tau)^T, f_d(\tau)^T)^T$  but the 18-DOF vector representation was more intuitive to debug. We will use the  $\mathbf{G}$  matrix to obtain  $f_d(\tau)$  from  $f_f(\tau)$  later.

define a new composite Jacobian,  $\mathbf{J}$ , force vector,  $\mathbf{f}$ , and task acceleration,  $\ddot{\mathbf{x}}$ , as

$$\mathbf{J} = \begin{pmatrix} J_a \\ J_f \end{pmatrix}, \quad \mathbf{f} = \begin{pmatrix} f_a \\ f_f \end{pmatrix}, \quad \ddot{\mathbf{x}} = \begin{pmatrix} \ddot{x}_a \\ \ddot{x}_f \end{pmatrix}. \quad (35)$$

Beginning with the physical equations (30) and (31), we can reformat the dynamics of the robot as a matrix equality with an analytic solution,

$$\begin{pmatrix} M_e & \mathbf{J}^T \\ \mathbf{J} & 0 \end{pmatrix} \begin{pmatrix} \ddot{q} \\ -\mathbf{f} \end{pmatrix} = \begin{pmatrix} -B_e - g_e \\ \ddot{\mathbf{x}} - \dot{\mathbf{J}}\dot{q} \end{pmatrix} + \begin{pmatrix} S \\ 0 \end{pmatrix} \tau, \quad (36)$$

which can be solved as in (23). The  $S$  matrix represents the under-actuation due to the floating base (under-actuation due to non-actuated mechanical joints is handled separately, through joint torque limits). We define the dynamically consistent pseudo inverse of  $\mathbf{J}^T$ ,  $\bar{\mathbf{J}}^T$ , satisfying  $\bar{\mathbf{J}}^T \mathbf{J}^T = I$  (a left inverse), but likely *not* satisfying  $\mathbf{J}^T \bar{\mathbf{J}}^T = I$ :

$$\bar{\mathbf{J}}^T = (\mathbf{J} M_e^{-1} \mathbf{J}^T)^{-1} \mathbf{J} M_e^{-1}. \quad (37)$$

And we define inertia in the composite task frame  $\Lambda = (\mathbf{J} M_e^{-1} \mathbf{J}^T)^{-1}$ . Together, these allow us to state the result,

$$\mathbf{f} = \Lambda \ddot{\mathbf{x}} - \Lambda \dot{\mathbf{J}} \dot{q} + \bar{\mathbf{J}}^T (B_e + g_e) - \bar{\mathbf{J}}^T S \tau. \quad (38)$$

Some terms in the previous expression are more significant than others, and some of the less significant terms are also corrupted by both imperfect knowledge of the robot’s mass matrix and (filtered) differentiation noise inherent in using quantized position sensors to estimate velocity and acceleration estimates. We did not notice a significant drawback in switching to a simplified version which represents a steady state equilibrium:

$$\mathbf{f} = \bar{\mathbf{J}}^T (g_e - S \tau). \quad (39)$$

Of course, if we moved fast enough, these omissions would be noticeable. With this simplification, swinging the swing foot very fast should require the operator to resist the centrifugal extension of the knee due to the inertia of the exoskeleton. Also, squatting very quickly should result in a non-zero backpack sensor force due to the neglected acceleration terms. However, at the speeds we tested these effects were dwarfed by other control and mechanical imperfections. We hope that future exoskeletons will achieve such mastery over the basic terms that these dynamic terms will regain relevancy.

#### E. A Linear Program for Shared-Body Control

At this point, we can express the optimization problem that the shared-body controller needs to solve at every controller update. Note that the passive joints<sup>9</sup> are treated as being active joints for the purpose of the optimization. Their non-zero torques represent the expectation of the exoskeleton on the human operator.

<sup>9</sup>The exoskeleton has 2 passive DOFs per leg: ankle inversion/eversion (ankle roll) and internal/external rotation of the hip (hip yaw).

We write our optimization problem,

$$\underset{\tau, s_+, s_-}{\text{minimize}} \quad w^T s_+ + w^T s_- \quad (40a)$$

$$\text{subject to} \quad C_r f_r(\tau) \geq 0, \quad (40b)$$

$$\tau \leq \bar{\tau}, \quad -\tau \leq \bar{\tau}, \quad (40c)$$

$$s_+ \geq e(\tau), \quad s_+ \geq 0, \quad (40d)$$

$$s_- \geq -e(\tau), \quad s_- \geq 0, \quad (40e)$$

with some new notation from Tab. IV. Slack variables  $s_+$  and  $s_-$  are introduced to describe absolute value operations. Weightings  $w$  form the weighted 1-norm cost. Limits on absolute torque are expressed with  $\bar{\tau}$ . And the  $\tau$ -dependent vector  $f(\tau)$  from (38) (or from the steady-state approximation (39)) is used to find  $e(\tau)$  and  $f_r(\tau)$ .

The first,  $e(\tau)$ , represents the 12-DOF vector of task errors for the *amplification task* and *inter-foot force task*:

$$e(\tau) = \begin{pmatrix} f_d(\tau) \\ f_a(\tau) - f_d \end{pmatrix}, \quad (41)$$

where  $f_d^d$  is the desired amplification task force from (17) in Sec. III-F;  $f_a(\tau)$  is the force the robot applies at the backpack interface, which is a part of  $f(\tau)$  as written in (35); and  $f_d(\tau)$  is also related to  $f(\tau)$  as in (28):

$$\begin{pmatrix} f_s(\tau) \\ f_d(\tau) \end{pmatrix} = \mathbf{G}^{-1} f_f(\tau), \quad (42)$$

using the matrix  $\mathbf{G}$  from (29).

The second,  $f_r(\tau)$ , represents the subset of the foot forces  $f_f(\tau)$  corresponding to the feet that are actually on the ground. This vector is used to compute the constraints associated with hard friction cones and unilateral contacts—i.e. (32), which is directly reproduced in (40b).

We call this program “Shared-Body Control” because the human and the robot’s torque and contact forces are both relevant. The true conditions for tipping over the foot are a function of both human and exoskeleton reaction forces. The sum of the human and robot reaction forces needs to lie within the friction cone, but sometimes the human works to counterbalance large torques the robot applies to the ground. We cannot know the human forces given our sensor configuration, so we are forced to be either optimistic (risking failure) or very conservative. Taking the conservative route means that our constraint will occasionally interfere with our tasks unnecessarily.

The human is also the only possible source of torques for the passive joints. By relaxing the torque requirements on the passive joints, the optimization will produce a torque vector representing a sum of exoskeleton and human originated torques. While we cannot expect the human to implement such torques, we can use this technique to prevent the exoskeleton from abandoning tasks which it could accomplish with help from the human (bounded, of course, by  $\bar{\tau}$ ).

## VI. IMPLEMENTATION IN HARDWARE

Implementing the control framework into a physical lower-body exoskeleton allows us to demonstrate both amplification and footstep transitions.



Fig. 5. The Apptronik Sagittarius Exoskeleton used in this paper. The operator can climb stairs with the exoskeleton, even when it is not amplifying forces, due to the backdrivable torque-controlled actuators (gravity compensation and strength amplification are both active in the pictured movement). Coloring segregates rigid exoskeleton parts for the right leg (blue-through-purple), human interfaces (orange) and the safety features (red).

### A. Hardware

Our hardware platform is the Sagittarius P5 lower-body exoskeleton from Apptronik Systems, shown in Fig. 5. This exoskeleton has 12 joints, six per leg. We name the joints in the serial kinematic chain from the torso to the foot 1) hip abduction/adduction, 2) hip flexion/extension, 3) hip internal/external rotation (hip yaw), 4) knee flexion/extension, 5) ankle flexion/extension, and 6) ankle pronation/supination (ankle roll). Of these six, four are powered joints. The two passive joints are hip internal/external rotation (also referred to as hip yaw for alignment with the local z axis) and ankle pronation/supination (which we also call ankle roll for similar reasons). The powered hip abduction and hip flexion joints are actuated by rotary series elastic actuators, while the other two feature proprietary linkage designs connecting linear series elastic actuators with rotary joint motion. Power is provided from off-board the device via a joint power and communication tether. The actuators communicate with a realtime Linux desktop workstation through an ethercat bus.

The different parts of the exoskeleton are highlighted in Fig. 5, with rigid bodies being bordered by different color lines on the spectrum from blue to purple, human attachment points in orange, and safety features in red. To ensure the safety of the operator, the exoskeleton is attached via a slack safety rope to an overhead gantry system, and the rope’s height is operated by an assistant when the height is changing rapidly (as in the stair-climbing activities pictured in Fig. 5. The operator wears a helmet, and there are multiple easy ways to stop the exoskeleton in an emergency: 1) a software emergency stop button, 2) a button on the top of the main backpack circuitry box, and 3) a button that the operator is required to hold at all times.

### B. Controller Implementation

While we have presented the controller design in a very general way, not all of its nuanced behavior is relevant enough

to demand implementation in the hardware system we used. In particular, the dynamic terms in (38) were not large enough for the operator to notice their omission, and the dynamically consistent pseudo-inversion of  $\mathbf{J}$  is unnecessary given that  $\mathbf{J}$  is invertible with the tasks we defined, thus

$$\mathbf{f} = \mathbf{J}^{-T}(\mathbf{g}_e - S\tau). \quad (43)$$

Note that when a component of the *amplification task* has  $K(s)$  set to zero, it will not amplify human forces but will still compensate gravity.

To summarize the tasks of the controller, the six individual spatial force vector components of the human-side force are fed into a diagonal matrix of amplification compensators as described in Sec. III. And this occurs in the frame of the *amplification task*—the hip frame. For the three sagittal plane forces and torques ( $x$ -force,  $z$ -force, and  $y$ -torque) we may apply non-zero amplification, but the other three are left at zero in this work. This is based on the physical intuition that the sagittal plane forces and torque represent the larger interaction quantities during walking. This forms the 6-DOF *amplification task*. Based on a bed of 12 insole-mounted pressure sensitive resistors, a rough estimate of the human center of pressure is produced. This estimate is used to construct the elements of the *inter-foot force task*, which is also a 6-DOF task. With this hardware-specific pre-processing completed, the tasks are sent to a separate and more generic module to perform the linear programming optimization work. The software implementation of this optimization process is separate from the Apptronik control framework and is available as open source software [52]. It primarily acts as a wrapper layer for the linear programming solver from the COIN-OR [53] community.

Fig. 6 describes the sensor configuration on the Sagit exoskeleton and contrasts this to the way we visualize the behavior of the optimization problem. Fig. 6.a shows the HCRL logo wearing the exoskeleton, colored dark gray for the structure of the exoskeleton, yellow for the visible force sensors, and green for the parts of the exoskeleton that are considered to be part of the human (the human attachments). In Fig. 6.b only the exoskeleton and the sensors are displayed, revealing the shoe inserts, with sensorized pads and an additional force sensor on the back. In Fig. 6.c we label the three human attachments as they are numbered in the code. Fig. 6.d introduces the visualization of the optimization configuration, where the operator (without its mass) and the exoskeleton are grounded at attachments which happen to correspond to the human interfaces. With the exoskeleton and massless operator hanging from these grounding points, the job of the exoskeleton is to choose the joint torques that minimize some cost, and this cost essentially identifies two groundings to avoid using (Fig. 6.e). For example, if the steady state amplification rate is non-amplifying, i.e.  $\alpha_0 = 1$ , then the *amplification task* directly penalizes the 1-norm of forces on ground 0—the fictitious connection between the exoskeleton and the world at the backpack. When the human's weight is on the left foot (interface 1) the foot cost penalizes the 1-norm of ground 2—the right foot's friction grounding, resulting in the robot deciding to support its weight as far as possible from ground 1—the left foot. The significance of the massless

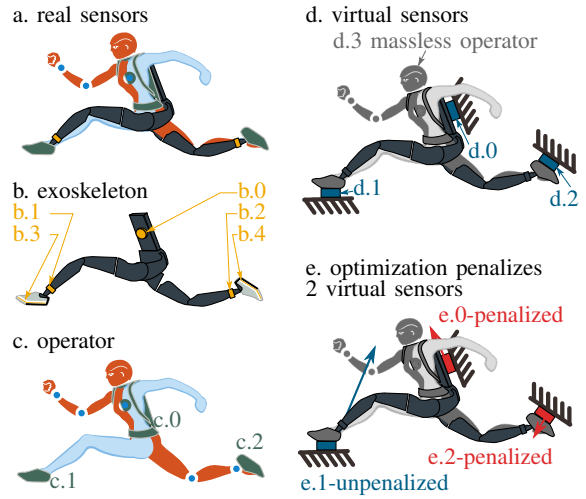


Fig. 6. To visualize our optimization problem's behavior, we consider our exoskeleton (a) and the difference between its real force sensor configuration (shown in b) and the three human interfaces the optimizer cares about (shown in c). The optimizer treats the operator as massless and assumes the three interfaces are contact constraints (d). The optimizer is aware of the mapping between the exoskeleton joint torque vector and the reaction forces at the three constraints. With the exoskeleton and massless operator hanging from these grounding points, the job of the optimizer is to choose the joint torques that minimize the cost function, and this cost essentially identifies two groundings to avoid using (Fig. 6.e). The result is that the cost function guides the exoskeleton to support the system's weight from the stance foot, at least when this does not conflict with the foot contact constraints or joint torque limits. While not explicitly pictured, the *amplification task* simply shifts the “zero” point for the cost function's penalty on the e.0 contact (measured by the b.0 force/torque sensor, and felt by the operator through the c.0 backpack attachment).

operator is that the optimization gives an allowance for the human to help the shared-control system exceed the limitations of the robot's own actuators. This means the robot is unlikely to abandon part of a task simply due to the passive joints, but it will if achieving this task would put unreasonably high strain on the human's ankle roll and hip yaw joints.

### C. Priorities

We iterated various priority rankings between the components of the *amplification task* until our operator was satisfied with the behavior. First, we attempted to re-create linear inverted pendulum behavior by prioritizing the moment components over the force components. This prioritization had been effective with the Hume biped robot [40]. Unfortunately, this first approach frustrated the operator, as the exoskeleton was naturally unstable. We eventually settled on the weightings in Tab. V, which sacrifice  $x$ -torque first and are more comfortable for the operator. This preference may be exoskeleton or operator specific. The main drawback of the priorities from Tab. V is that at each stance transition the hips of the device roll such that the stance hip is higher than the swing hip—likely due to the lower penalty on hip amplification  $x$ -torque. However, we must sacrifice something, and this appeared to be the least-uncomfortable choice. The large swing in the hip position is due to the rather loose coupling that the backpack provides in this degree of freedom.

TABLE V  
IMPLEMENTED TASK PRIORITIES

Task	Weighting
Hip Amplification $x$ -Force	$1 \times 10^5$
Hip Amplification $y$ -Force	$1 \times 10^5$
Hip Amplification $z$ -Force	$1 \times 10^5$
Hip Amplification $x$ -Torque	$1 \times 10^0$
Hip Amplification $y$ -Torque	$1 \times 10^1$
Hip Amplification $z$ -Torque	$1 \times 10^5$
Inter-Foot $x$ -Force, Limit Penalty	$1 \times 10^{-1}, 1 \times 10^5$
Inter-Foot $y$ -Force, Limit Penalty	$1 \times 10^{-1}, 1 \times 10^5$
Inter-Foot $z$ -Force, Limit Penalty	$1 \times 10^{-6}, 1 \times 10^6$
Inter-Foot $x$ -Torque, Limit Penalty	$1 \times 10^{-6}, 1 \times 10^5$
Inter-Foot $y$ -Torque, Limit Penalty	$1 \times 10^{-6}, 1 \times 10^5$
Inter-Foot $z$ -Torque, Limit Penalty	$1 \times 10^0, 1 \times 10^5$

In testing, we began to suspect that operators may prefer a lower task penalty on the *inter-foot force task* while in double support but react strongly negatively to *inter-foot force task* violation while in swing (since this entails the exoskeleton loading their swing foot). We made a slight modification to the sum scalarized cost for the *inter-foot force task* as described in (40a), (40d), (40e), and (41). A second copy of the task penalty was added, with a dead zone. We made the *inter-foot force task* error appear *twice* in the task error vector  $e(\tau)$  instead of only once as in (41). Thus, we had two separate components of the weight vector  $w$  from (40a) that penalized the same task. To introduce the dead zone for the second copy of the penalty, we added a sparse bias vector to (40d) and (40e). We call this new penalty, with its dead zone and higher penalty cost, the “Limit Penalty” (see Tab. V) since it acts like a soft limit forcing the values to stay within the dead zone. Within the dead zone, this new cost still behaves like the original weighted 1-norm cost (plus a constant bias that does not influence the optimum), but at the boundary of the dead zone, the weight suddenly becomes much higher.

We scheduled the dead zone width based on the center of pressure location, such that in single support this dead zone collapsed to zero and the *inter-foot force task* essentially took on the higher weighting of the limit penalty. In dual support, the width of the dead zone reached its widest when the feet were evenly balanced and reduced linearly in either direction away from that midpoint.

#### D. Demonstrating the Amplification Task

We conducted a set of simple tests to demonstrate the difference between gravity compensation and human strength amplification. These tests aimed to demonstrate an improvement in amplification stability relative to previous controllers developed for the exoskeleton and its previous partial prototypes (the 1-DOF testbed from [31], [38], a two degree of freedom leg, and a previous revision on the same lower-body design) under the same project [12], which was a condition of our using the exoskeleton.<sup>10</sup>

Fig. 7 and Tab. VI show the basic structure of our tests: the operator wears the exoskeleton in a roughly standing position

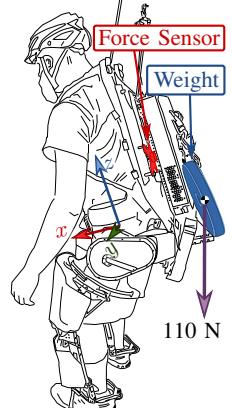
<sup>10</sup>Which is to say, our testing time was limited, and the scope of our experiments was narrow.

TABLE VI  
EXPERIMENTAL PARAMETERS

Test	SBC <sup>†</sup>	$\alpha_0$	Load
VI-D.1	Off	0	0 N
VI-D.2	On	0	0 N
VI-D.3	On	0	110 N
VI-D.4	On	3	110 N

†—Shared-Body Controller (SBC) enabled.

Fig. 7. Load position in VI-D.3 and VI-D.4. Load hangs from a chain attached to the exoskeleton. Human effort measured with a six-axis force torque sensor, highlighted in red. Measurements are presented in the pictured “hip center” coordinate frame.



and various controller features are turned on and off. Extra weight is attached to the backpack as an unknown load in tests VI-D.3-4, and the image shows where it hangs relative to the operator. Fig. 8 shows the results of the three tests.

#### E. Discussion of The Amplification Task

In the first test, VI-D.1 the exoskeleton joints are on, but the desired torque is zero. The first column of plots in Fig. 8 show the large  $z$ -force on the backpack due to the gravitational load of the exoskeleton acting on the operator. Variation in the angle shows that the operator was not perfectly holding still over the duration of the test. This, while it prevents us from easily comparing across experiments (the operator does not even have the same resting posture between loading configurations) is hard to compensate for or avoid.

The next test, VI-D.2 enables gravity compensation—which means the torques from the shared-body controller are applied to the robot, but the amplification filters are all set to apply no strength amplification feedback ( $\alpha_0 = 1$ , so  $f_a^d = 0$ ). This drastically reduces, but does not entirely eliminate, the interface forces and torques. Even if the robot’s mass parameters were perfectly modeled, the operator would still need to apply forces through this interface to control the passive joints of the robot. Compensating for the weight of the heavy exoskeleton is the most significant component of the system’s behavior. We can see this from the enormous reduction in human interface forces and torques in Fig. 8 between VI-D.1 and VI-D.2: the vertical force,  $F_z$ , drops roughly 300 Newtons, and the sagittal plane torque,  $T_y$ , drops roughly 40 Newton meters.

In test VI-D.3, we added an 11 Kg (25 lb) mass to the backpack, without changing the control mode. Based on our empirical determination, this represents the maximum load the exoskeleton could reliably handle without overheating during dynamic motions like walking. The test does not focus on the transient response but on the steady state behavior with the weight (mechanically, it would be hard to make the weight addition appear sudden without dropping it).

We see some unexpected behavior in the vertical sensor force: the weight’s 110 N did not transfer to the sensorized interface. The user confirmed that additional vertical force and sagittal torque were felt. This suggests a “force leak” in

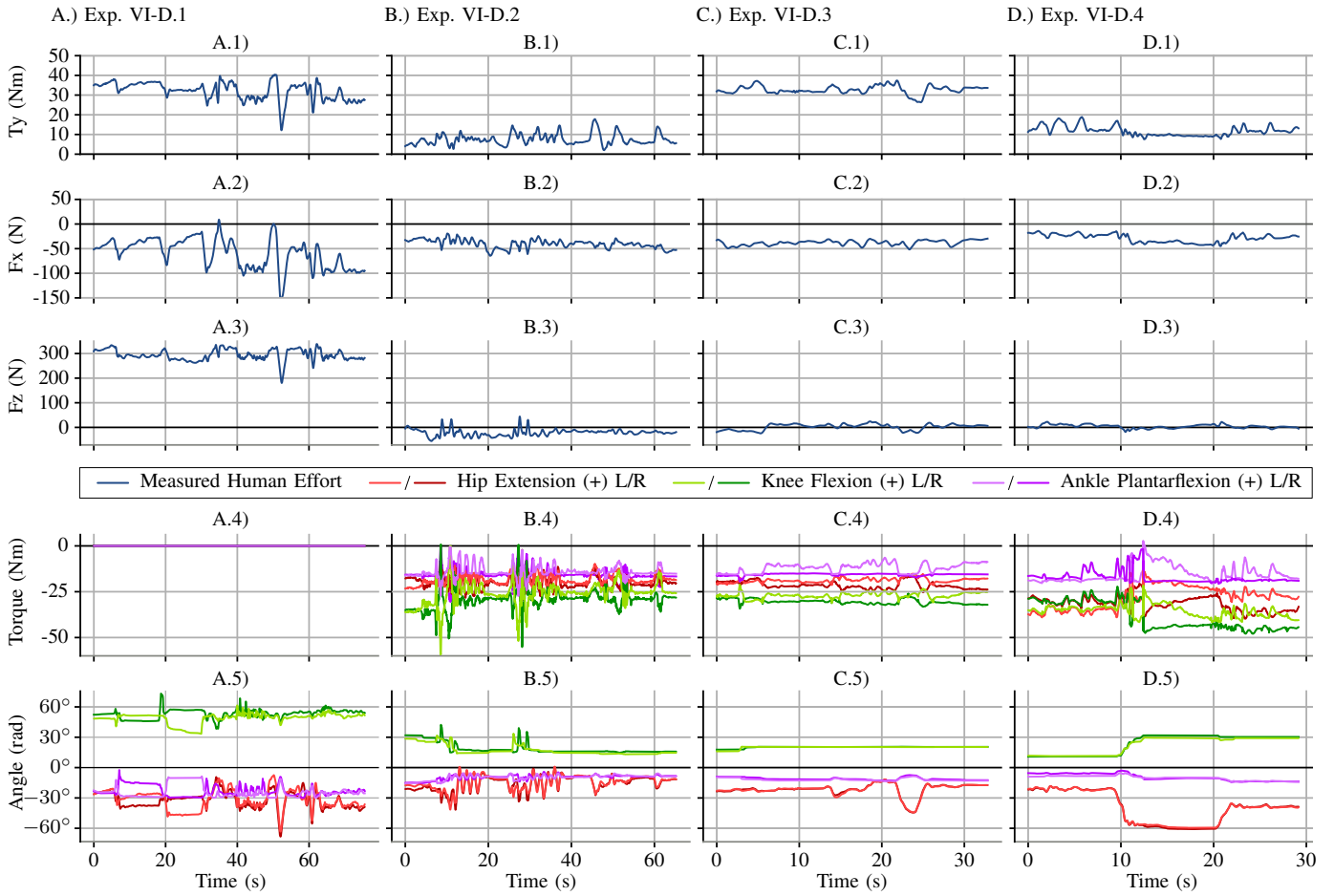


Fig. 8. The four experiments from Tab. VI, shown as subfigure columns A–D, are compared in terms of the three sagittal plane components of the human–robot interaction force/torque, the sagittal joint torques, and the sagittal joint angles. In Exp. VI-D.1 (A), the exoskeleton joints apply no torque (as shown in A.4), and the human–robot interface supports  $\approx 300$  N (as shown in A.3) as well as a  $\approx 35$  Nm moment at the hip (as shown in A.1). In Exp. VI-D.2 (B), the controller is turned on with  $\alpha_0 = 1$  (no amplification), and human–robot vertical force (B.3) and sagittal torque (B.1) are vastly decreased due to gravity compensation. In Exp. VI-D.3 (C), a 11 kg mass is attached to the back of the exoskeleton (as shown in Fig. 7), and this produces an increase in the human–robot sagittal torque (C.1),  $\approx 30$  Nm. Finally, Exp. VI-D.4 (D) increases  $\alpha_0$  from 1 (no amplification) to 3 in the sagittal tasks, and the human–robot sagittal torque increase due to the added mass is reduced by roughly a third—considering B.1, C.1, and D.1 representing the average numerical value of the curves,  $D.1 - B.1 \approx 1/3(C.1 - B.1)$ —as expected. With the amplification engaged, the operator deepens the squat at 10 seconds (D.5) and then moves to a second, less extreme squat at 20 seconds (D.5), showing that the torque reduction continues to work. This squat is shown in the video attachment [54]. We would also expect that amplification would reduce the vertical force from the added mass; however, the vertical force remains roughly zero before adding the weight (B.3), after adding the weight (C.3), and with both the weight and amplification (D.3)—the expected 110 N force increase between (B.3) and (C.3) did not occur. Since the operator recalls feeling vertical forces from the addition of the mass, we suspect that there is a “force leak” where the vertical component transferred to the operator in a way the force sensor could not detect. Torque and angle measurements in the bottom two subfigure rows are measured using the robot’s spring deflection encoders and joint encoders, and therefore represent the robot’s—and not the operator’s—torque and position.

the design of the backpack sensor, where the force of the added weight is transferred to the operator without passing through the sensor. A likely culprit is the hip-pad of the backpack (directly connected to the operator) and the hips of the exoskeleton—as this would be consistent with the clear increase in the  $y$ -torque. The “force leak” does not appear to allow all vertical forces to bypass the sensor. VI-D.1 clearly shows large forces.

In the final test, VI-D.4, we engaged the amplification filters—providing a steady state amplification factor of 3, and a zero pair at 1 Hz for all three degrees of freedom in the sagittal plane. By choosing these conservative settings, we were able to achieve stability on the first try.<sup>11</sup>

<sup>11</sup>A later gain-tuning experiment revealed that the bandwidth limit is higher than this, but we ran out of time for exhaustive identification of this limit.

Our system is pioneering in that it amplifies human strength at the backpack/hip link of the exoskeleton; there are no direct performance comparisons for this control feature. Our steady state amplification of human forces by 300% exceeded the 208% amplification (52% mass reduction) of sagittal hip moment in [55], which also used force feedback to amplify human lower-body strength. However, this is not an exact comparison, as [55]’s system used a treadmill mounted exoskeleton, had a different sensing configuration, and has only two degrees of freedom whereas our system has 12. The amplification’s pole frequency (.58 Hz) and amplification magnitude ( $\alpha_0 = 3$ ) at the hip/backpack human–robot interface are comparable to our previous results on a 1-DOF human elbow exoskeleton; in the notation of Appendix A, [31]’s robust controller used  $\alpha_0 = 10$ ,  $k_G = 0.1$ ,  $Z_g = 10$ , and  $P_g = 0.01$ , resulting



Fig. 9. Frames from the demo. Frames a.1-5: climbing stairs with amplification but no added weight. Frames b.1-5: walking around. Frames c.1-3: walking around with amplification and extra weight.

in an amplification magnitude of 2.995 at 0.58 Hz. However, unlike our controller, [31] had even greater amplification at lower frequencies: its lowest pole-pair was at 0.146 Hz, and its steady state amplification rate was 9.91.

As shown in Fig. 8’s fourth column, the human’s effort was reduced to roughly a third of its value in the third column in the  $y$ -torque component. More specifically, the disturbance due to the added weight, which can be seen by comparing VI-D.3 (with weight) against VI-D.2 (no weight) in terms of  $y$ -axis torque, is attenuated by the amplification factor, resulting in a much smaller disturbance effect when comparing VI-D.4 (attenuated weight) to VI-D.2 (no weight). We must make this comparison despite joint angle differences on the order of 10 degrees between these tests—a limitation of our operator and operator-robot coupling. In VI-D.4, the operator engages in two different squat positions (switching posture at roughly 10 and 20 seconds). The interface forces remain within 10-15 Nm despite these kinematic changes. This supports the notion that if the operator were able to perfectly reproduce the posture from Exp. VI-D.3 in VI-D.4, the  $y$ -axis torque would also be within this range.

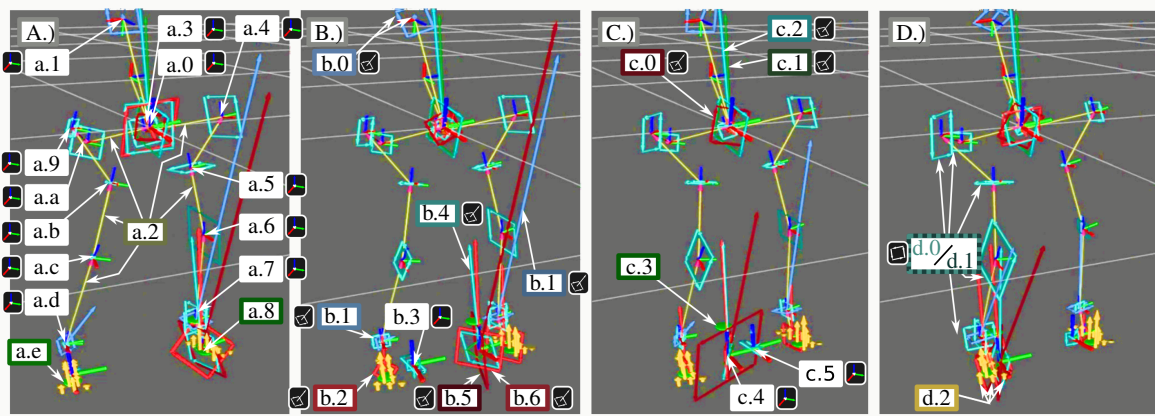
#### F. Discussion of Foot Transitions

Distributing weight between the two feet using the *inter-foot force task* is a key behavior of the system and was tested when the operator walked on level ground and stairs. Since the robot itself was based on high bandwidth torque-controlled actuation, the operator could easily backdrive it to climb up stairs or to stand on one foot. While this happened, the exoskeleton continued to compensate for its own gravitational weight and amplify strength at the hip/backpack sensor.

Fig. 9.b and Fig. 10 show the operator shifting weight from one foot to another and lifting up the legs one at a time.

This behavior highlights the human-led foot contact transitions and demonstrates how the weight is shifting in *anticipation* of the actual contact transition. As mentioned in Sec. IV, the weighting matrices  $Q_1$  and  $Q_2$  in (20) are scheduled according to the robot’s measurement of the human’s weight distribution. When the human shifts weight to one foot, the  $Q$  matrix penalty for reaction forces on the other foot becomes much larger. And since this causes the COP of the robot to approximate the COP of the human, this prevents the human from needing to lift a load-bearing robot leg. In addition, the penalty limit method allowed the exoskeleton more freedom during dual support but smoothly reduced this freedom when approaching single support, so that by the time it was reached the *inter-foot force task* was essentially the highest priority.

This behavior is shown in more detail through the internal robot visualization of Fig. 10. This Rviz model manages to show almost everything that is going on, as described in the legend table. All frames are expressed as red ( $x$ ) green ( $y$ ) blue ( $z$ ) line segments meeting at the local origin. Spatial force vectors (comprising a force and a torque) are shown as a ray from the local origin (the force) and a bi-vector—a directed plane comprised of four vectors making a square—to represent the torque. Joint torques are represented as pure bi-vectors. Unlike vector descriptions of torque, the bi-vector visualization has an unambiguous scaling relative to the force visualizations and cannot be confused for them. The four instants pictured in Fig. 10 of the contact transition show the apparent center of pressure moving from the left foot to the right foot, and the corresponding shift in all the joint torques and the predicted reaction forces from the shared-body controller. As this is shifting, the reference frame of expression for the sum of reaction forces and the *inter-foot force task*’s difference of reaction forces swap feet. At all



Callout	Description	Callout	Description
a.0	The base or hip frame	b.2	Optimal reaction SFV for the right foot
a.1	The frame of the backpack's force/torque sensor	b.3	Frame of the representation for the inter-foot SFV
a.2	Visualization of child frame to parent frame vectors	b.4	Robot contribution to optimal sum SFV
a.3	(Obscured) frame of the left hip adductor joint	b.5	Measured sum SFV (from structural sensors)
a.9	(Clearly visible) frame of the right hip adductor joint	b.6	Optimal sum SFV
a.4/a.a	Frame of the left/right hip flexor joint	c.0	Measured backpack SFV in hip frame
a.5/a.b	Frame of the left/right passive hip "yaw" joint	c.1	Robot gravity SFV visualization
a.6/a.c	Frame of the left/right knee flexion joint	c.2	Robot gravity compensation SFV visualization
a.7/a.d	Frames of the left/right ankle flexion and passive ankle roll joints (hard to distinguish)	c.3	Measured human COP (ankle origin weighted average)
a.8/a.e	Frame of representation for the constructed sum/difference reaction force vectors—momentarily coincident with the (not visualized) left/right foot bottom frame due to single support	c.4	Frame of rep. for sum SFV
b.0	Spatial force vector (SFV) of the backpack force/torque sensor	c.5	Frame of rep. for inter-foot SFV
b.1	SFVs of the left and right foot structural force/torque sensors, expressed in the ankle frame	d.0	Optimal robot joint torques
		d.1	Applied robot joint torques (filtered and saturated)
		d.2	Individual FSR relative magnitude visualization for the 12 sensors of each foot, used to estimate within-foot center of pressure

Fig. 10. Human weight transfer in 0.2 seconds (subfigures evenly spaced in time) showing the exoskeleton visualization in the rviz program.

times, the reaction force/torque b.6 representing the sum is roughly equal to the sum ground reaction force calculated without using the passive joints b.4—which means that the robot is supporting the vast majority of its weight even during this transition. The backpack force/torque sensor b.0 confirms this, as it is small (and therefore hard to spot) throughout the transition.

## VII. DISCUSSION

Strength amplification control offers us the potential to feel stronger as we manipulate the environment (including the loads) through our exoskeleton. This paper provides a framework that has put that vision into practice under laboratory circumstances, albeit with an exoskeleton that was not originally designed to manipulate the environment.

### A. Benefits and Drawbacks

This framework has several advantages relative to the state of the art. It respects contact limitations—guaranteeing that the exoskeleton will never force the person to roll their ankles, lift their toes, or slide their feet. It improves human-side compliance relative to the gravity compensation baseline without the anti-stable acceleration feedback of [8]. It keeps the human in control of the inter-foot force distribution using an elegant linear algebraic decomposition of the contact forces—a more general approach than Ref. [17]. It allows the operator to move heavy objects without removing the force-feedback path

that they would need in order to move the objects carefully—a force-feedback path that is removed by admittance control strategies [16].

Of course, the framework has downsides as well. The strategy depends on centralizing the contact between the human and the exoskeleton into a small set of sensors.<sup>12</sup> This centralization places a significant burden on the mechanical design and introduces a new failure mode—the “force leak,” where interaction between the robot and the operator occurs outside the sensors. Additionally, all amplified interaction with the environment must go through the exoskeleton structure—another mechanical design challenge. Due to the complexity of the mechanical design problem, the strategy makes it difficult to achieve the ultra-high energy density of successful locomotion augmentation exoskeletons [56], [5]. This is an open problem. Augmentation exoskeletons are already close to the energy-density boundary at which the energy they provide is equal to the energy they cost the user due to their mass. The extra design constraints make it harder for amplification exoskeletons to cross this boundary even at slow walking speeds.

### B. Open Problems in the Control Framework

The control framework itself also has some open questions. First, we approximated the mechanical impedance of the human and the cuff as being component-wise decoupled between

<sup>12</sup>With one foot on the ground, our exoskeleton measures the human at two places: the hip/backpack attachment and the swing foot attachment.

the six degrees of freedom in our *amplification task*. Since an extremely low amplification bandwidth is still stable, and since our tuning process increases bandwidth until instability is discovered, this approximation limits us by introducing conservatism in the final tuning. Because of inter-component human coupling behavior, the tuning process may result in a different answer depending on the order with which the individual task sub-component bandwidths are tuned.

Second, the framework was only tested with six *amplification task* sub-components. In theory, it supports arbitrarily many task sub-components. And it is also theoretically possible to join the *inter-foot force task* with the *amplification task*—to make the swing foot capable of acting like an amplified manipulator. We lacked the sensing configuration for such a test: it would require the full 6-DOF interaction force/torque between the human foot and the exoskeleton foot to be measured, rather than just the vertical pressure between them. Thus, to validate the scalability our theory predicts, we would need an exoskeleton with either A) more sensorized human contacts (arms, for example) or B) the elimination of all human–environment contact that does not pass through the exoskeleton as an intermediary.

Third, the controller tuning process is intended to be robust to all activities the operator performs, but we cannot know all these activities beforehand. A practical extension to this work would be to introduce an always-online learning process to continually adapt the tuning and avoid instability. Previously we have looked at tuning automation using online stiffness estimation [57]. However, this type of automation could potentially be simpler: if the system starts to vibrate, it could reduce the amplification bandwidth until the vibration subsides. This is essentially how we tuned the system manually.

On the other hand, higher performance might be obtained with a more complex strategy: modeling the human and redesigning the controller. Modeling the human online could draw on convex programs that automatically learn bounded-uncertainty models [58]. With this more versatile system identification approach, even a human stiffness with ‘off-diagonal’ terms could be learned. With every change to the model of the human stiffness bounds, robust control theory could synthesize a transfer matrix  $\mathbf{K}(s)$  that guarantees stability.

Finally, the approach makes an assumption that a foot is always on the ground—and this precludes interesting applications in free-fall, underwater (with neutral buoyancy), or micro-gravity. In such circumstances, the *amplification task* and *inter-foot force task* structures would need to be combined together and significantly altered. A “virtual single foot contact” would not exist. In its place, the *change in centroidal momentum* [46] would need to become the component of torque-space left intentionally unconstrained by the tasks. The remaining DOFs in torque-space would then be the subject of the new combined amplification task. The assignment of intuitive and easy-to-tune amplification controllers to such a task—which would concern an ever-changing subspace of the end-effector contact force space—is an open problem. However, the approach to parameterizing the *internal forces of multi-contact* from [39] would be a reasonable starting point.

### C. Series Elastic Actuators

Our exoskeleton hardware features series elastic actuators that are force/torque-controlled, and this decision also comes with benefits and drawbacks. To our knowledge, this paper is the first demonstration of Multi-DOF amplification control based on human interface force sensors and actuator force sensors (i.e. the series elastic elements). While such actuators are commonly used in wearable robots, they are a key part of our strategy, because with them we can avoid sensorizing the external force interface. This is a major advantage compared to systems designed to follow the extender concept [22]. The lack of environment sensors gives us the freedom to properly handle amplification for environmental contact forces at any contact point along the structure of the exoskeleton (or at least in double support—we would need to amplify the *inter-foot force task* to amplify contact between the environment and the swing leg).

As for series compliance itself, however, control performance would be slightly better off with nearly-rigid springs. The series elastic actuators are simply torque sources to us, and direct drive motors offer higher bandwidth as torque sources. Removing the springs could also save weight. But series elasticity has some practical advantages: the force sensing is cheap and high quality, the robot’s motors are protected from impacts, and both the transmission’s friction and the rotor’s reflected inertia are well hidden from the user.

### D. Potential Applications

We have demonstrated the control framework on the Apptronik Sagittarius exoskeleton, which is designed to lift heavy body-distributed payloads as the user moves quickly. In this use case, the benefit of amplification control—relative to gravity compensation of the payload—is the potential reduction of inertial forces the user needs to compensate (without resorting to acceleration feedback) and the forces due to modeling error in the compensation. But this is not necessarily the most impactful application area for amplification as a technology.

To really see the potential of amplification, we would need to imagine an exoskeleton that was built for heavy-duty environmental manipulation. Such a system would need to move very slowly but with very high forces. If it were to move fast, it would require significantly more impressive power density than we typically see today. Such an exoskeleton, worn by a skilled operator, might be fielded in difficult terrain as an alternative to tracked construction vehicles, with specialized tools for manipulating the environment. These tools might be so massive that there exists no viable alternative for using them in unstructured environments. The exoskeleton would act as an adjustable bracing system that allows the operator to maneuver them into position. Perhaps the operator is a sculptor who uses the exoskeleton to lug a massive jackhammer up the mountainside in order to carve an ornamented staircase for tourists. Or maybe a forestry service worker is using it to operate a chainsaw at the end of a 24-foot telescoping pole. Exoskeletons as platforms opens up the door to new industrial tools and potential job sites—all because they combine the maneuverability of people with the strength of machines.

Our exoskeleton is designed to mimic the kinematics of the person wearing it, but this is not the only way to go about the design. The control framework also has the potential to allow non-anthropomorphic legged robots to amplify human interaction. Imagine, for example, a robot connected to an operator's feet with long spindly legs that join together at a robot 'hip'. This hip also features an enormous power tool that requires the user to manipulate it with both hands. This architecture would require the same control system features as our anthropomorphic exoskeleton structure: strength amplification in the frame of the robot's hip, awareness of contact inequalities, and human-led footstep transitions.

## APPENDIX A RELATION TO THE CONTROLLER DESIGN OF [31]

The control strategy we previously published in [31] can also be re-expressed in terms of an amplification transfer function. Ref. [31] explored the creation of amplification controllers based on reduction of an "ideal amplification error signal"  $Y(s) = (\alpha_0 - 1)F_H(s) - \eta(s)F_A(s)$  (in the notation of Sec. III) using a feedback compensator  $G(s)$ , with desired actuator force  $F_A(s) = G(s)Y(s)$ . This left us with a feedback stability model that required system identification of the human. Our proposed structure for  $G(s)$  was that of a first order lag filter. The purpose of this section is to explain this prior approach in terms of the modified human-side compliance.

We can eliminate the self-referential  $F_A(s)$  definition using algebra:

$$F_A(s) = G(s)((\alpha_0 - 1)F_H(s) - \eta(s)F_A(s)), \quad (44)$$

$$F_A(s) = \frac{G(s)(\alpha_0 - 1)}{(1 + G(s)\eta(s))} F_H(s). \quad (45)$$

We also have a first order lag model of  $G(s)$ ,

$$G(s) = \frac{s + z_G}{s + p_G} k_G, \quad (46)$$

where  $k_G$  is the gain,  $z_G$  is the zero frequency, and  $p_G$  is the pole frequency for the lag. We can therefore express the equivalent  $K(s)$  this strategy is implementing,

$$K(s) = \frac{s + z_G}{s/k_G + p_G/k_G + (s + z_G)\eta(s)} (\alpha_0 - 1). \quad (47)$$

From here, we can see that the strategy results in something close to another lag filter (if we neglect the actuator dynamics to treat  $\eta(s) \approx 1$ ). However, in this case the nominal amplification of the strategy is

$$\alpha(s) = \frac{(\alpha_0 + 1/k_G)s + (\alpha_0 z_G + p_G/k_G)}{(1 + 1/k_G)s + (z_G + p_G/k_G)}, \quad (48)$$

which is similar to the controller parameterization in this paper, but less convenient because its steady state behavior is not  $\alpha_0$  as we might expect but rather  $\frac{\alpha_0 + p_G/(k_G z_G)}{1 + p_G/(k_G z_G)}$ , which will always be less than or equal to  $\alpha_0$ . Nor does it return to the natural system behavior at high frequencies, since the nominal value of high frequency  $\alpha(s)$  does not return to unity. (In practice it will still return to unity due to  $\eta(s)$ ).

## ACKNOWLEDGMENT

For this research in human strength amplification, Apptronik Systems Inc. provided, at no cost, access to their exoskeleton hardware called Sagit-P5. They also provided mechanical maintenance and improvements to the low level interfaces to facilitate the testing. The authors would like to thank Donghyun Kim for providing insights on contact transitions. This system was designed and built by a team including Jonas Fox, Brad Resh, Uday Savaria, Ryan Harkins, Ryan MacWilliams, Joel Cox, and Paul Fleury. The authors would also like to acknowledge Bill Helmsing and Jeff Cardenas for allocating time for our research on the Sagit-P5 exoskeleton.

This work was supported in part by NASA grant NNX15AQ33H "Controlling Robots with a Spring in Their Step," for which Gray Thomas is the fellow and Luis Sentis is the advisor.

## REFERENCES

- [1] H. K. Kwa, J. H. Noorden, M. Missel, T. Craig, J. E. Pratt, and P. D. Neuhaus, "Development of the IHMC mobility assist exoskeleton," in *Robotics and Automation (ICRA), 2009 IEEE International Conference on*. IEEE, 2009, pp. 2556–2562.
- [2] O. Harib, A. Hereid, A. Agrawal, T. Gurriet, S. Finet, G. Boeris, A. Duburcq, M. E. Mungai, M. Masselin, A. D. Ames, K. Sreenath, and J. W. Grizzle, "Feedback control of an exoskeleton for paraplegics: Toward robustly stable, hands-free dynamic walking," *IEEE Control Systems Magazine*, vol. 38, no. 6, pp. 61–87, 2018.
- [3] T. G. Sugar, J. He, E. J. Koeneman, J. B. Koeneman, R. Herman, H. Huang, R. S. Schultz, D. Herring, J. Wanberg, S. Balasubramanian *et al.*, "Design and control of RUPERT: a device for robotic upper extremity repetitive therapy," *IEEE transactions on neural systems and rehabilitation engineering*, vol. 15, no. 3, pp. 336–346, 2007.
- [4] B. Kim and A. D. Deshpande, "An upper-body rehabilitation exoskeleton harmony with an anatomical shoulder mechanism: Design, modeling, control, and performance evaluation," *The International Journal of Robotics Research*, vol. 36, no. 4, pp. 414–435, 2017.
- [5] L. M. Mooney, E. J. Rouse, and H. M. Herr, "Autonomous exoskeleton reduces metabolic cost of human walking during load carriage," *Journal of neuroengineering and rehabilitation*, vol. 11, no. 1, p. 80, 2014.
- [6] J. Zhang, P. Fiers, K. A. Witte, R. W. Jackson, K. L. Poggensee, C. G. Atkeson, and S. H. Collins, "Human-in-the-loop optimization of exoskeleton assistance during walking," *Science*, vol. 356, no. 6344, pp. 1280–1284, 2017.
- [7] S. Lee, J. Kim, L. Baker, A. Long, N. Karavas, N. Menard, I. Galiana, and C. J. Walsh, "Autonomous multi-joint soft exosuit with augmentation-power-based control parameter tuning reduces energy cost of loaded walking," *Journal of Neuroengineering and Rehabilitation*, vol. 15, no. 1, p. 66, 2018.
- [8] H. Kazerooni, J.-L. Racine, L. Huang, and R. Steger, "On the control of the berkeley lower extremity exoskeleton (BLEEX)," in *Robotics and Automation (ICRA), 2005 IEEE International Conference on*. IEEE, 2005, pp. 4353–4360.
- [9] K. Kong, H. Moon, D. Jeon, and M. Tomizuka, "Control of an exoskeleton for realization of aquatic therapy effects," *IEEE/ASME Transactions on Mechatronics*, vol. 15, no. 2, pp. 191–200, 2010.
- [10] G. Lv, H. Zhu, and R. D. Gregg, "On the design and control of highly backdrivable lower-limb exoskeletons: A discussion of past and ongoing work," *IEEE Control Systems Magazine*, vol. 38, no. 6, pp. 88–113, 2018.
- [11] J. Lin, G. Lv, and R. D. Gregg, "Contact-invariant total energy shaping control for powered exoskeletons," in *2019 American Control Conference (ACC)*. AACC, 2019, pp. 664–670.
- [12] O. H. Campbell, IV, "Framework for full body augmentative exoskeleton control," Master's thesis, The University of Texas at Austin, 2018.
- [13] H. Kazerooni, "Exoskeletons for human power augmentation," in *Intelligent Robots and Systems (IROS), 2005 IEEE/RSJ International Conference on*. IEEE, 2005, pp. 3459–3464.
- [14] K. Kong and M. Tomizuka, "Control of exoskeletons inspired by fictitious gain in human model," *IEEE/ASME Transactions on Mechatronics*, vol. 14, no. 6, pp. 689–698, 2009.

- [15] W. Yu and J. Rosen, "Neural PID control of robot manipulators with application to an upper limb exoskeleton," *IEEE Transactions on Cybernetics*, vol. 43, no. 2, pp. 673–684, 2013.
- [16] M. Fontana, R. Vertechy, S. Marcheschi, F. Salsedo, and M. Bergamasco, "The body extender: A full-body exoskeleton for the transport and handling of heavy loads," *IEEE Robotics & Automation Magazine*, vol. 21, no. 4, pp. 34–44, 2014.
- [17] S. C. Jacobsen and M. X. Olivier, "Contact displacement actuator system," September 2014, US Patent 8,849,457.
- [18] A. Lecours, B. M. St-Onge, and C. Gosselin, "Variable admittance control of a four-degree-of-freedom intelligent assist device," in *Robotics and Automation (ICRA), 2012 IEEE International Conference on*. IEEE, 2012, pp. 3903–3908.
- [19] H. Kawamoto and Y. Sankai, "Power assist method based on phase sequence and muscle force condition for hal," *Advanced Robotics*, vol. 19, no. 7, pp. 717–734, 2005.
- [20] A. J. Young and D. P. Ferris, "State of the art and future directions for lower limb robotic exoskeletons," *IEEE Transactions on Neural Systems and Rehabilitation Engineering*, vol. 25, no. 2, pp. 171–182, 2016.
- [21] D. J. Gonzalez and H. H. Asada, "Hybrid open-loop closed-loop control of coupled human–robot balance during assisted stance transition with extra robotic legs," *IEEE Robotics and Automation Letters*, vol. 4, no. 2, pp. 1676–1683, 2019.
- [22] H. Kazerooni and J. Guo, "Human extenders," *Journal of Dynamic Systems, Measurement, and Control*, vol. 115, no. 2B, pp. 281–290, 1993.
- [23] H. Kazerooni and S. Mahoney, "Dynamics and control of robotic systems worn by humans," in *Proceedings. 1991 IEEE International Conference on Robotics and Automation*. IEEE, 1991, pp. 2399–2405.
- [24] H. Kazerooni and S. L. Mahoney, "Dynamics and control of robotic systems worn by humans," *Journal of Dynamic Systems, Measurement, and Control*, vol. 113, no. 3, pp. 379–387, 09 1991. [Online]. Available: <https://doi.org/10.1115/1.2896421>
- [25] J. B. Makinson, D. P. Bodine, and B. R. Fick, "Machine augmentation of human strength and endurance Hardiman I prototype project," Specialty Materials Handling Products Operation, General Electric Company, Tech. Rep., 1969.
- [26] N. Paine, S. Oh, and L. Sentis, "Design and control considerations for high-performance series elastic actuators," *IEEE/ASME Transactions on Mechatronics*, vol. 19, no. 3, pp. 1080–1091, 2014.
- [27] N. A. Paine, "High-performance series elastic actuation," Ph.D. dissertation, The University of Texas at Austin, 2014.
- [28] S. P. Buerger and N. Hogan, "Complementary stability and loop shaping for improved human–robot interaction," *IEEE Transactions on Robotics*, vol. 23, no. 2, pp. 232–244, April 2007.
- [29] H. Kazerooni, "Human–robot interaction via the transfer of power and information signals," *IEEE Transactions on Systems, Man, and Cybernetics*, vol. 20, no. 2, pp. 450–463, 1990.
- [30] S. P. Buerger and N. Hogan, "Relaxing passivity for human–robot interaction," in *Intelligent Robots and Systems (IROS), 2006 IEEE/RSJ International Conference on*. IEEE, 2006, pp. 4570–4575.
- [31] B. He, G. C. Thomas, N. Paine, and L. Sentis, "Modeling and loop shaping of single-joint amplification exoskeleton with contact sensing and series elastic actuation," in *2019 Annual American Control Conference (ACC)*, AACC. IEEE, July 2019, pp. 4580–4587.
- [32] B. He, H. Huang, G. C. Thomas, and L. Sentis, "Complex stiffness model of physical human–robot interaction: Implications for control of performance augmentation exoskeletons," in *2019 IEEE/RSJ International Conference on Intelligent Robots and Systems (IROS)*. IEEE, 2019, pp. 6748–6755.
- [33] N. Hogan, "Adaptive control of mechanical impedance by coactivation of antagonist muscles," *IEEE Transactions on Automatic Control*, vol. 29, no. 8, pp. 681–690, 1984.
- [34] J. E. Colgate and N. Hogan, "Robust control of dynamically interacting systems," *International Journal of Control*, vol. 48, no. 1, pp. 65–88, 1988.
- [35] N. Hogan, "Controlling impedance at the man/machine interface," in *Robotics and Automation (ICRA), 1989 IEEE International Conference on*. IEEE, 1989, pp. 1626–1631.
- [36] J. E. Colgate and J. M. Brown, "Factors affecting the z-width of a haptic display," in *Robotics and Automation, 1994. Proceedings., 1994 IEEE International Conference on*. IEEE, 1994, pp. 3205–3210.
- [37] R. J. Adams and B. Hannaford, "Stable haptic interaction with virtual environments," *IEEE Transactions on Robotics and Automation*, vol. 15, no. 3, pp. 465–474, 1999.
- [38] G. C. Thomas, J. M. Coholich, and L. Sentis, "Compliance shaping for control of strength amplification exoskeletons with elastic cuffs," in *Proceedings of the 2019 IEEE/ASME International Conference on Advanced Intelligent Mechatronics*. IEEE and ASME, July 2019, pp. 1199–1206.
- [39] L. Sentis, J. Park, and O. Khatib, "Compliant control of multicontact and center-of-mass behaviors in humanoid robots," *Robotics, IEEE Transactions on*, vol. 26, no. 3, pp. 483–501, 2010.
- [40] D. Kim, Y. Zhao, G. C. Thomas, B. R. Fernandez, and L. Sentis, "Stabilizing series-elastic point-foot bipeds using whole-body operational space control," *IEEE Transactions on Robotics*, vol. 32, no. 6, pp. 1362–1379, 2016.
- [41] N. A. Radford, P. Strawser, K. Hambuchen, J. S. Mehling, W. K. Verdeyen, A. S. Donnan, J. Holley, J. Sanchez, V. Nguyen, L. Bridgwater et al., "Valkyrie: NASA's first bipedal humanoid robot," *Journal of Field Robotics*, vol. 32, no. 3, pp. 397–419, 2015.
- [42] N. Paine, J. S. Mehling, J. Holley, N. A. Radford, G. Johnson, C.-L. Fok, and L. Sentis, "Actuator control for the NASA-JSC Valkyrie humanoid robot: A decoupled dynamics approach for torque control of series elastic robots," *Journal of Field Robotics*, vol. 32, no. 3, pp. 378–396, 2015.
- [43] R. Featherstone, *Rigid body dynamics algorithms*. Springer, 2014.
- [44] G. F. Franklin, J. D. Powell, and A. Emami-Naeini, *Feedback control of dynamic systems*. Addison-Wesley Reading, MA, 1994, vol. 3.
- [45] G. C. Thomas, J. Mehling, J. Holley, and L. Sentis, "Phase-relaxed-passive full state feedback gain limits for series elastic actuators," 2020, unpublished.
- [46] T. Koolen, S. Bertrand, G. C. Thomas, T. De Boer, T. Wu, J. Smith, J. Englsberger, and J. Pratt, "Design of a momentum-based control framework and application to the humanoid robot Atlas," *International Journal of Humanoid Robotics*, vol. 13, no. 01, p. 1650007, 2016.
- [47] B. J. Stephens and C. G. Atkeson, "Dynamic balance force control for compliant humanoid robots," in *2010 IEEE/RSJ International Conference on Intelligent Robots and Systems*, Oct 2010, pp. 1248–1255.
- [48] D. Kim, S. J. Jorgensen, H. Hwang, and L. Sentis, "Control scheme and uncertainty considerations for dynamic balancing of passive-ankled bipeds and full humanoids," in *2018 IEEE-RAS 18th International Conference on Humanoid Robots (Humanoids)*. IEEE, 2018, pp. 1–9.
- [49] T. Bretl and S. Lall, "Testing static equilibrium for legged robots," *IEEE Transactions on Robotics*, vol. 24, no. 4, pp. 794–807, 2008.
- [50] K. Bouyarmane and A. Kheddar, "On weight-prioritized multitask control of humanoid robots," *IEEE Transactions on Automatic Control*, vol. 63, no. 6, pp. 1632–1647, 2017.
- [51] E. J. Candes, M. B. Wakin, and S. P. Boyd, "Enhancing sparsity by reweighted  $\ell_1$  minimization," *Journal of Fourier analysis and applications*, vol. 14, no. 5–6, pp. 877–905, 2008.
- [52] G. C. Thomas. (2019) LP Exo: A free implementation of a 1-norm prioritized whole body controller. GitHub. [Online]. Available: [https://bitbucket.org/gray\\_thomas/exo\\_lp.git](https://bitbucket.org/gray_thomas/exo_lp.git)
- [53] R. Lougee-Heimer, "The common optimization interface for operations research: Promoting open-source software in the operations research community," *IBM Journal of Research and Development*, vol. 47, no. 1, pp. 57–66, 2003.
- [54] G. C. Thomas. (2020) Implementation of "an amplification shaping framework for exoskeletal human strength augmentation". YouTube. [Online]. Available: [https://youtu.be/rcDMHYgGV\\_4](https://youtu.be/rcDMHYgGV_4)
- [55] D. Zanotto, Y. Akiyama, P. Stegall, and S. K. Agrawal, "Knee joint misalignment in exoskeletons for the lower extremities: Effects on user's gait," *IEEE Transactions on Robotics*, vol. 31, no. 4, pp. 978–987, 2015.
- [56] J. Kim, G. Lee, R. Heimgartner, D. Arumukhom Revi, N. Karavas, D. Nathanson, I. Galiana, A. Eckert-Erdheim, P. Murphy, D. Perry, N. Menard, D. K. Choe, P. Malcolm, and C. J. Walsh, "Reducing the metabolic rate of walking and running with a versatile, portable exosuit," *Science*, vol. 365, no. 6454, pp. 668–672, 2019. [Online]. Available: <https://science.sciencemag.org/content/365/6454/668>
- [57] H. Huang, H. Cappel, G. C. Thomas, B. He, and L. Sentis, in *2020 Annual American Control Conference (ACC)*, AACC. IEEE, 2020, pp. 5131–5138.
- [58] G. C. Thomas and L. Sentis, "Quadric inclusion programs: an lmi approach to  $\mathcal{H}_\infty$ -model identification," *IEEE Transactions on Automatic Control*, vol. 64, no. 10, pp. 4229–4236, 2019. [Online]. Available: <http://dx.doi.org/10.1109/TAC.2019.2897886>
- [59] G. C. Thomas, B. He, and L. Sentis, "Safety control synthesis with input limits: a hybrid approach," in *2018 Annual American Control Conference (ACC)*. AACC, June 2018, pp. 792–797.